

The Quantum Kicked Rotor: A Paradigm of Quantum Chaos. Foundational aspects and new perspectives

Giuliano Benenti^{a,b}, Giulio Casati^{a,c}, Jiangbin Gong^{d,e,f} and Zhixing Zou^{d,f}

^aUniversità degli Studi dell'Insubria, Center for Nonlinear and Complex Systems, Dipartimento di Scienza e Alta Tecnologia, via Valleggio 11, 22100 Como, Italy

^bIstituto Nazionale di Fisica Nucleare, Sezione di Milano, via Celoria 16, 20133 Milano, Italy

^cFederal University of Rio Grande do Norte, International Institute of Physics, Campus Universitário - Lagoa Nova, CP. 1613, Natal, Rio Grande Do Norte 59078-970, Brazil

^dNational University of Singapore, Department of Physics, Singapore

^eMajuLab, CNRS-UCA-SU-NUS-NTU International Joint Research Unit, Singapore

^fNational University of Singapore, Centre for Quantum Technologies, Singapore

© 20xx Elsevier Ltd. All rights reserved.

Chapter Article tagline: ???, 2025

Keywords

Time scales of quantum chaos, correspondence principle, dynamical localization, quantum resonances, topological aspects in variants of kicked rotor, coupled kicked rotors, non-Hermitian kicked rotor

Abstract

The kicked rotor provides a simple yet powerful model for introducing many of the central concepts of classical and quantum chaos. Despite its apparent simplicity, it exhibits rich dynamical behavior and has found applications across a wide range of fields, including atomic and optical physics, condensed matter physics, and emerging quantum technologies. This chapter begins by exploring foundational ideas using the kicked rotor as a unifying framework. We first discuss the transition from regular to chaotic motion in the classical system, and then introduce key quantum phenomena such as dynamical localization and quantum resonances. Special attention is devoted to the emergence of characteristic time scales and their role in the quantum–classical correspondence. To make these ideas more concrete, we also provide a brief overview of experimental realizations of the kicked rotor and its variants, illustrating how theoretical concepts are implemented in practice. In the second part of the chapter, we guide the reader toward more recent and advanced developments. Topics include near-resonant dynamics, topological features of kicked systems, the emergence of quantum dynamical phases inferred from classical transport properties, and extensions to non-Hermitian physics. We conclude with a discussion of open problems and future perspectives, outlining directions in which the kicked rotor continues to offer valuable insights.

1 Introduction

The general mathematical theory of dynamical systems—most notably ergodic theory [1]—has its historical roots in classical mechanics. Its scope, however, is by no means confined to that setting and extends to a much broader class of phenomena, including systems governed by quantum mechanics. This immediately raises a fundamental question: how can classical dynamical chaos be understood within the framework of quantum mechanics?

In classical systems, chaos originates from strong local instabilities of motion, typically characterized by an exponential sensitivity to initial conditions. As a consequence, trajectories governed by deterministic equations become effectively unpredictable and exhibit behavior that appears random. The term chaotic thus refers precisely to this loss of predictability: for almost all trajectories, reliable long-term prediction becomes impossible. This notion can be formalized within the algorithmic theory of dynamical systems through the Alekseev–Brudno theorem (see Ref. [2]). According to this theorem, the information content $I(t)$ associated with a trajectory segment of length t —defined as the number of bits required to describe the orbit up to time t , or equivalently the length of the shortest program capable of reproducing those t steps—grows asymptotically as

$$I(t) \sim h_{\text{KS}} |t|, \quad (1)$$

where h_{KS} is the Kolmogorov–Sinai (KS) entropy, equal to the sum of all positive Lyapunov exponents [3].

This result implies that predicting a new segment of a chaotic trajectory requires an amount of new information proportional to the length of that segment, independently of the previous history of the motion. In other words, no information about the future can be extracted from past observations: the future cannot be inferred from the past. This intrinsic unpredictability is the defining characteristic of chaotic dynamics. By contrast, if the instability of motion grows only algebraically (i.e., sub-exponentially), the amount of new information required per unit time decreases with the length of the already known trajectory. In this case, the predictability improves with time, and asymptotically the dynamics becomes

predictable.

It is important to emphasize, however, that short-term prediction is always possible, even in chaotic systems. This is true within a finite predictability window, $r < 1$, where

$$r = \frac{h_{\text{KS}} |t|}{|\ln \mu|}. \quad (2)$$

Here μ denotes the accuracy with which the trajectory is recorded. The regime $r \gg 1$ corresponds to effectively random behavior, where predictability is lost.

Exponential instability is typically associated with a continuous spectrum of motion, which in turn leads to the decay of correlations—a crucial prerequisite for the applicability of statistical descriptions. By contrast, systems with a discrete spectrum can exhibit at most linear instability in time [4]. Local exponential instability therefore defines a limiting regime known as dynamical chaos. The opposite limiting case is that of regular (integrable) motion, characterized by a discrete spectrum. This dichotomy poses a serious challenge for the understanding of quantum chaos. Indeed, for any quantum system whose motion is bounded in phase space, both the energy and frequency spectra are necessarily discrete. According to the classical theory of dynamical systems, such behavior corresponds to the limiting case of regular motion and thus appears to be fundamentally incompatible with chaos.

The ultimate origin of this fundamental quantum property lies in the discreteness of phase space itself, which is a direct consequence of the Heisenberg uncertainty principle. This principle enforces a finite minimal volume for any elementary phase-space cell and underlies the entire structure of quantum mechanics. It is important to emphasize that the linearity of the Schrödinger equation is not directly relevant in this context. The requirement of nonlinearity for classical chaos pertains specifically to the trajectory-based description of motion, where nonlinearity is essential to confine otherwise linearly unstable trajectories. Indeed, the classical Liouville equation governing the evolution of phase-space distributions is itself linear. In mixing systems, any smooth distribution function relaxes, on average, toward a stationary state. This relaxation process is time-reversible, just as the underlying microscopic dynamics is. There is, however, a crucial distinction: while the phase-space distribution does not recur, individual trajectories recur infinitely many times—irrespective of whether the motion is regular or chaotic.

The time reversibility of the distribution function is associated with the increasingly complex structure it develops during relaxation. In the presence of exponential instability, the characteristic spatial scale of the oscillations in the distribution function decreases exponentially with time. The memory of the initial state is encoded in these progressively finer phase-space structures—a mechanism that relies fundamentally on the continuity of phase space.

To conclude, two properties are crucial for dynamical chaos in classical mechanics: a continuous spectrum of motion and a continuous phase space. Both of these properties are absent in quantum mechanics. On the other hand the correspondence principle requires transition from quantum to classical mechanics for all phenomena including dynamical chaos.

A resolution of this apparent contradiction (*ad maiorem correspondentiae principii gloriam*¹) is to focus on finite-time statistical properties. The key observation is that the distinction between discrete and continuous spectra becomes unambiguous only in the infinite-time limit. This insight already emerged in the earliest numerical studies of quantum chaos [5], most notably through the introduction of a remarkably simple model: the kicked rotor.

The structure of this chapter reflects the progressive broadening of the kicked rotor’s conceptual and physical scope across several areas of modern physics. We begin by recalling its foundational role as a paradigmatic model of classical and quantum chaos, where it provides deep insight into the characteristic time scales governing quantum chaotic dynamics. These include the short Ehrenfest time, after which a quantum wave packet spreads significantly and no longer follows classical trajectories, and the longer localization time, beyond which quantum interference suppresses classical diffusion. We then emphasize its profound connection to Anderson localization, which established the model as a bridge between dynamical systems and disordered quantum transport. Building on this legacy, we survey a selection of advances that illustrate how the model has evolved into a versatile platform for exploring a wide spectrum of contemporary problems.

We begin with the single-particle Hermitian framework, including its semiclassical description, which continues to provide essential intuition linking phase-space structures to quantum interference phenomena. We then discuss representative single-particle generalizations, such as doubled kicking protocols, different kicking potentials, and spinful extensions. These developments demonstrate how the model naturally connects to central themes in modern condensed-matter and Floquet physics, including topological phases, Anderson transitions, and quantum Hall physics. The chapter subsequently turns to coupled kicked rotors, which constitute a natural Hermitian many-body extension and offer a controlled setting for investigating the dynamics of entanglement and the emergence of complexity in interacting driven systems. Finally, we address non-Hermitian generalizations, an increasingly active research direction motivated by the growing interest in open quantum systems. Owing to the remarkable breadth and rapid expansion of the field, our treatment in each section is necessarily selective; rather than aiming at exhaustive coverage, we highlight key conceptual developments and emerging perspectives shaping current research.

¹For the greater glory of the correspondence principle. In a letter from Heisenberg to Pauli, September 30, 1924.

2 Foundational aspects

2.1 Classical kicked rotor

The kicked rotor belongs to the class of periodically driven dynamical systems and is governed by the Hamiltonian

$$H(\theta, I; \tau) = \frac{I^2}{2} + V(\theta) \sum_{j=-\infty}^{+\infty} \delta(\tau - jT), \quad (3)$$

where (I, θ) are conjugate action-angle variables, with $0 \leq \theta < 2\pi$. This Hamiltonian consists of two terms, $H(\theta, I; \tau) = H_0(I) + U(\theta; t)$, where $H_0(I) = I^2/2$ corresponds to the kinetic energy of a free rotor—a particle moving on a circle parametrized by the coordinate θ —while

$$U(\theta; t) = V(\theta) \sum_j \delta(\tau - jT) \quad (4)$$

represents a driving force that acts on the particle instantaneously at discrete time intervals T . Therefore, we say that the dynamics described by Hamiltonian (3) is kicked. The corresponding Hamiltonian equations of motion are given by

$$\begin{cases} \dot{I} = -\frac{\partial H}{\partial \theta} = -\frac{dV(\theta)}{d\theta} \sum_{j=-\infty}^{+\infty} \delta(\tau - jT), \\ \dot{\theta} = \frac{\partial H}{\partial I} = I. \end{cases} \quad (5)$$

These equations can be integrated straightforwardly, yielding a stroboscopic map that describes the evolution from time lT^- (just before the l -th kick) to time $(l+1)T^-$ (just before the $(l+1)$ -th kick):

$$\begin{cases} \bar{I} = I + F(\theta), \\ \bar{\theta} = \theta + T\bar{I}, \end{cases} \quad (6)$$

where $F(\theta) = -dV(\theta)/d\theta$ is the force acting on the particle. Note that the transformation $(\theta, I) \rightarrow (\bar{\theta}, \bar{I})$ is area-preserving, since the associated Jacobian determinant is equal to one.

In the following, we focus on the kicked rotor, for which $V(\theta) = k \cos \theta$, so that the force becomes $F(\theta) = -dV(\theta)/d\theta = k \sin \theta$. By rescaling the action (momentum) variable via $I \rightarrow J = TI$, the classical dynamics is seen to depend only on the single parameter $K = kT$. Indeed, in terms of the rescaled variables (J, θ) Eq. (6) becomes

$$\begin{cases} \bar{J} = J + K \sin \theta, \\ \bar{\theta} = \theta + \bar{J}. \end{cases}, \quad (7)$$

which is known as the Chirikov standard map [6, 7]. This map can be studied on the cylinder ($J \in (-\infty, +\infty)$), or on the torus $0 \leq J < 2\pi L$, where L is an integer (the integer condition ensures that no discontinuities are introduced in the second equation of Eq. (7) when J is taken modulo $2\pi L$). Due to its apparent simplicity and intrinsic richness, the standard map plays a key role in the study of both classical and quantum chaos. It can be interpreted as the Poincaré surface-of-section map for a conservative system with two degrees of freedom. What makes the standard map nearly universal is that it provides a local approximation (in momentum) for a broad class of dynamical systems. Notable examples include the photo-effect in Rydberg atoms [8, 9, 10, 11, 12] (see Sec. 2.5.1) and two-dimensional billiards [13, 14, 15, 16, 17], to name just a few.

For $K = 0$, the motion is integrable, with the action J being a constant of motion. The level curves, i.e., the lines $J(\theta) = J_0$, completely foliate the (θ, J) phase space. These are called invariant tori. On each torus, the motion is simply given by a rotation of θ with frequency $\omega = (\bar{\theta} - \theta)/T = J_0/T = I_0$. It is important to note that such rotations (or oscillations) are nonlinear, since their frequency depends on the action. It is this nonlinearity which is responsible for chaos. When the parameter K is nonzero but sufficiently small, the Kolmogorov–Arnold–Moser (KAM) theorem predicts that some invariant tori—with strongly irrational frequencies—persist, albeit in a deformed state [18, 19]. These surviving tori constrain the motion in J , a situation referred to as global stability. For rational values of $\omega/(2\pi/T) = p/q$ (that is, $J_0 = 2\pi p/q$), the corresponding tori are destroyed. In agreement with the Poincaré–Birkhoff theorem, of the infinite number of periodic trajectories that originally populated these tori, only $2q$ periodic points survive. These are fixed points of the map iterated q times. Half of these points are elliptic, while the other half are hyperbolic. This results in a mixed phase space, composed of chaotic regions and islands of stability (see panel (a) in Fig. 1). As K increases, more and more tori are destroyed by the perturbation. At a critical value $K = K_c \approx 0.97$ [20], even the last invariant tori break down, and the motion in J becomes unbounded (see panel (b) in Fig. 1). The fraction of phase space occupied by stability islands decreases with increasing K , and for $K \gtrsim 5$ it becomes negligible. The motion is then effectively fully chaotic and exhibits strong statistical properties, such as local instability, mixing, and rapid decay of correlations (see panel (c) in Fig. 1).

A less accurate but physically insightful estimate of K_c can be obtained using the Chirikov resonance-overlap criterion [6, 7].

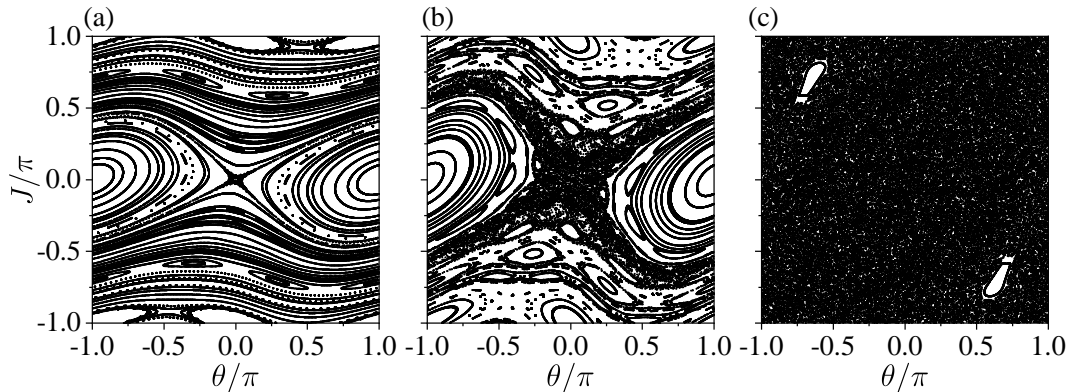


Fig. 1 Poincaré sections of the classical kicked rotor map (7) on the torus $\theta \in (-\pi, \pi]$, $J \in (-\pi, \pi]$, for different kicking strengths: (a) $K = 0.5$. (b) $K = 0.97$. (c) $K = 5$. These plots are stroboscopic maps obtained by iterating the standard map for different initial conditions. For $K = 0.5$, the phase space exhibits the main resonance at $(\theta, J) = (\pi, 0)$, an unstable fixed point at $(0, 0)$ asymptotic to the separatrix, additional stable islands associated with higher-order resonances, and deformed invariant tori that bound the motion in J . As the system becomes increasingly nonlinear, the last surviving of these invariant tori are destroyed at $K \approx 0.97$. Finally, for $K = 5$, the phase space is predominantly chaotic, with only small stability islands remaining.

In the context of the kicked rotor, we begin by applying the Poisson summation formula to the Dirac comb,

$$\sum_{j=-\infty}^{+\infty} \delta(\tau - jT) = \frac{1}{T} \left(1 + 2 \sum_{m=1}^{+\infty} \cos \frac{2\pi m\tau}{T} \right), \quad (8)$$

which allows the kicked-rotor Hamiltonian to be written as

$$H = \frac{J^2}{2} + K \sum_{m=-\infty}^{+\infty} \cos(\theta - 2\pi mt), \quad (9)$$

where $t \equiv \tau/T$ is a discrete time variable measured in units of map iterations. This Hamiltonian describes an infinite set of resonances located at $J_m = 2\pi m$. The spacing between neighboring resonances is therefore $\delta = 2\pi$. For each value of m , Eq. (9) corresponds to an effective pendulum, with a stable fixed point at $(\theta, J) = (\pi, 2\pi m)$ and an unstable fixed point at $(\theta, J) = (0, 2\pi m)$. The width of the associated separatrix is $\Delta J = 4\sqrt{K}$. According to the Chirikov criterion, the transition to global chaos occurs when adjacent resonances overlap, i.e., when $\Delta J/\delta > 1$. This condition yields $K > \frac{\pi^2}{4} \approx 2.5$. Although this argument neglects higher-order resonances at $J_{m\ell} = 2\pi m/\ell$ (with $\ell > 1$) and therefore overestimates the true critical value $K_c \approx 0.97$, it correctly captures the order of magnitude and provides an intuitive physical picture of the transition to chaos.

Local instability can be conveniently studied by linearizing around a reference trajectory θ_0 the standard map:

$$\begin{bmatrix} \delta\bar{J} \\ \delta\bar{\theta} \end{bmatrix} = M \begin{bmatrix} \delta J \\ \delta\theta \end{bmatrix} = \begin{bmatrix} 1 & K \cos \theta_0 \\ 1 & 1 + K \cos \theta_0 \end{bmatrix} \begin{bmatrix} \delta J \\ \delta\theta \end{bmatrix}. \quad (10)$$

The stability matrix M has eigenvalues

$$\mu_{\pm}(\theta_0) = 1 + \frac{K \cos \theta_0}{2} \pm \sqrt{K \cos \theta_0 \left(1 + \frac{K \cos \theta_0}{4} \right)}. \quad (11)$$

Note that the eigenvalues depend not only on K but also on θ_0 and this implies local fluctuations in the instability along a trajectory. To compute the maximum Lyapunov exponent λ we need to average $\ln|\mu_{+}|$ over the reference trajectory. For $K \gg 1$, the trajectory essentially fills the entire phase space and therefore λ is obtained after a phase averaging. i.e., averaging $\ln|\mu_{+}(\theta_0)| \approx \ln(K|\cos \theta_0|)$ over θ_0 , yielding

$$\lambda \approx \ln(K/2). \quad (12)$$

For any $K \gg 1$, the system exhibits normal diffusion in the momentum variable. Although the standard map is a deterministic system, the motion of a trajectory along the momentum direction becomes, in practice, indistinguishable from a random walk. As a result, the evolution of a distribution function $f(J, t)$ is governed by a Fokker-Planck equation:

$$\frac{\partial f}{\partial t} = \frac{\partial}{\partial J} \left(\frac{1}{2} D \frac{\partial f}{\partial J} \right). \quad (13)$$

Here t is the discrete time and the diffusion coefficient D is defined by

$$D = \lim_{t \rightarrow \infty} \frac{\langle (\Delta J(t))^2 \rangle}{t}, \quad (14)$$

where $\Delta J \equiv J - \langle J \rangle$ and $\langle \dots \rangle$ denotes the average over an ensemble of trajectories. If at time $t = 0$ we take a phase space distribution with initial momentum J_0 and random angles $0 \leq \theta < 2\pi$, then the solution of the Fokker–Planck equation (13) is given by

$$f(J, t) = \frac{1}{\sqrt{2\pi Dt}} \exp\left(-\frac{(J - J_0)^2}{2Dt}\right). \quad (15)$$

The width of this Gaussian distribution grows in time, according to

$$\langle (\Delta J(t))^2 \rangle \approx D(K)t. \quad (16)$$

For $K \gg 1$, the diffusion coefficient is well approximated by the random phase approximation, in which we assume that there are no correlations between the angles (phases) θ at different times. Hence, we have

$$D(K) \approx \frac{1}{2\pi} \int_0^{2\pi} d\theta (\Delta J_1)^2 = \frac{1}{2\pi} \int_0^{2\pi} d\theta (K \sin \theta)^2 = \frac{K^2}{2}, \quad (17)$$

where $\Delta J_1 = \bar{J} - J$ is the change in action after a single map step ²

2.2 Quantum kicked rotor

The quantized standard map [5, 22] (or quantum kicked rotor) is obtained by applying the usual canonical quantization rules: $\theta \rightarrow \hat{\theta}$ and $I \rightarrow \hat{I} = -i\partial/\partial\theta$, where we set $\hbar = 1$. The quantum evolution over one map iteration, that is, over one period of the perturbations, is described by a unitary operator \hat{U} , known as the Floquet operator, which acts on the wave function ψ as follows:

$$\bar{\psi} = \hat{U} \psi = \exp\left(-i \int_{IT^-}^{(l+1)T^-} d\tau \hat{H}(\theta, I; \tau)\right) \psi, \quad (18)$$

where H is Hamiltonian (3). Since the potential $V(\theta)$ is switched on only at discrete times lT , it is straightforward to obtain

$$\bar{\psi} = e^{-iT\hat{I}^2/2} e^{-iV(\hat{\theta})} \psi = e^{-iT\hat{I}^2/2} e^{-ik \cos \hat{\theta}} \psi = \hat{U}_T \hat{U}_k \psi. \quad (19)$$

The Floquet operator encapsulates all of the system's dynamical properties and is expressed as the product of two non-commuting unitary operators, representing the effect of a single kick (\hat{U}_k) and the free rotation (\hat{U}_T), respectively ³ Note that, due to quantization, the dynamics depends essentially on both parameters k and T , and not just on their product K . Since $[\hat{\theta}, \hat{J}] = [\hat{\theta}, T\hat{I}] = iT$, the effective Planck constant is given by $\hbar_{\text{eff}} = T$ and the classical limit corresponds to $T \rightarrow 0$ and $k \rightarrow \infty$ while keeping $K = kT$ constant.

Map (19) can be made explicit in the coordinate (angular) representation as follows:

$$\hat{U}_k = \exp(-ik \cos \theta), \quad \hat{U}_T = \exp\left(i\frac{T}{2} \frac{\partial^2}{\partial \theta^2}\right). \quad (20)$$

In the momentum representation, defined by the Fourier transform

$$\psi(\theta) = \sum_{n=-\infty}^{+\infty} A_n e^{in\theta}, \quad (21)$$

we obtain

$$\hat{U}_k = \sum_{m=-\infty}^{+\infty} (-i)^{n-m} J_{n-m}(k), \quad \hat{U}_T = \exp\left(-i\frac{T}{2} m^2\right), \quad (22)$$

where J_{n-m} are Bessel functions of the first kind. Since these functions rapidly decrease as the difference between the indices and the argument increases (for $|n - m| > k$), each kick couples approximately k momentum eigenstates (which are also eigenstates of the unperturbed evolution at $k = 0$).

²A more refined calculation [21], which takes into account phase correlations at different times, leads to $D(K) \approx \frac{K^2}{2} C(K)$, where the correlator is given by $C(K) \approx 1 - J_2(K)$, with J_2 denoting the Bessel function of the first kind of order 2. Note that $C(K) \rightarrow 1$ when $K \gg 1$, so that the random phase approximation is recovered in this limit.

³Although the operators \hat{U}_k and \hat{U}_T do not commute, exchanging them is simply equivalent to a shift in time. A symmetric splitting of the Floquet operator, $\hat{U} = \hat{U}_{T/2} \hat{U}_k \hat{U}_{T/2}$ is sometimes used.

2.2.1 Quantum resonances

Quantum evolution is governed by two distinct time scales: the first, T , corresponds to the period of the external perturbation; the second is 4π , which arises from the property of the angular momentum operator whose spectrum, for $k = 0$, consists of integers, i.e., $I_n = n$ (always at $\hbar = 1$). As a result, the Floquet operator remains unchanged under the transformation $T \rightarrow T + 4\pi$, see the expression for \hat{U}_T in Eq. (22). Therefore, without loss of generality one can restrict to $0 < T \leq 4\pi$. A resonance condition—without classical analogue—occurs when the ratio between the two characteristic time scales defined above is a rational number:

$$T = 4\pi \frac{p}{q}, \quad (23)$$

with p and q integer numbers. On physical grounds, this condition is equivalent to stating that the energy carried by an integer number of photons of the perturbation, each with energy $\hbar\omega = 2\pi\hbar/T$, exactly matches the energy required for a transitions between levels of the unperturbed rotor, whose eigenenergies are $E_n = n^2\hbar^2/2$. In this case, the rotor's average energy grows quadratically in time. The average energy after t kicks is given by

$$E(t) = \frac{1}{2\pi} \int_0^{2\pi} d\theta \psi^*(\theta, tT) \left(-\frac{1}{2} \frac{\partial^2}{\partial \theta^2} \right) \psi(\theta, tT), \quad (24)$$

Choosing $a \equiv p/q = 1$, the wavefunction at time tT takes the form

$$\psi(\theta, tT) = \exp(-ikn \cos \theta) \psi(\theta, 0), \quad (25)$$

from which it follows that

$$E(t) \sim \frac{k^2}{4} n^2, \quad \text{as } n \rightarrow \infty. \quad (26)$$

This quadratic energy growth can be demonstrated for any rational value of a [23, 24], with the exception of the case $a = 1/2$, for which the dynamics is strictly periodic: $\hat{U}^2 = \hat{I}$. On the other hand, numerical evidence [23, 25] strongly suggests that the timescale over which resonant energy growth becomes observable increases extremely rapidly with q . In the general case where $T/(4\pi)$ is irrational, the phenomenon of dynamical localization—to be discussed later—emerges.

2.3 The quantum kicked rotor and the correspondence principle

The kicked rotor serves as an ideal model for illustrating the characteristic time scales of quantum chaos—up to which phenomena such as exponential instability and diffusion can be recovered, in accordance with the correspondence principle.

2.3.1 Ehrenfest time scale

In order to understand the existence of different time scales in quantum motion, we compare the classical and quantum evolution starting from the same initial conditions. According to the Ehrenfest theorem, a quantum wave packet follows a bundle of classical trajectories as long as the packet remains sufficiently narrow. During this interval, the quantum evolution is exponentially unstable and appears random, mirroring the behavior of the underlying classical dynamics.

However, the initial size of the quantum wave packet is bounded from below by the elementary quantum phase-space cell, which is of order \hbar . Let us consider an initial minimum-uncertainty wave packet of size $\Delta\theta_0\Delta J_0 = T\Delta\theta_0\Delta I_0 \sim T\hbar_{\text{eff}}$, with $\Delta\theta_0 \sim \Delta J_0 \sim \sqrt{\hbar_{\text{eff}}}$, which corresponds to the optimal, least-spreading wave packet. Due to classical exponential instability, the angular spread grows as $\Delta\theta(t) \sim \Delta\theta_0 \exp(\lambda t) \sim \sqrt{\hbar_{\text{eff}}} e^{\lambda t}$, where λ is the maximum Lyapunov exponent of the system. Complete spreading over the angle variable θ occurs after the so-called Ehrenfest time scale:

$$t_E \sim \frac{1}{\lambda} \ln \left(\frac{1}{\hbar_{\text{eff}}} \right) \sim \frac{|\ln T|}{\ln(K/2)}. \quad (27)$$

Thus, true dynamical chaos, characterized by exponential sensitivity to initial conditions, is limited in quantum mechanics (for Hamiltonian systems) to the logarithmically short Ehrenfest time scale. This phenomenon was first discussed in detail in Ref. [26]. Note that t_E increases indefinitely as $\hbar_{\text{eff}} \rightarrow 0$, in agreement with the correspondence principle.

2.3.2 Heisenberg time scale and dynamical localization

The second characteristic time scale, t^* —often referred to as the Heisenberg time—marks the point at which the quantum evolution begins to diverge from classical diffusion. This departure is associated with the phenomenon of quantum dynamical localization, first observed in [5].

For times $t > t^*$, while the classical distribution continues to diffuse indefinitely, the quantum distribution instead reaches a stationary state. This steady state is exponentially localized in the momentum eigenbasis, as illustrated in Figs. 2 and 3:

$$W_m \equiv |\langle m | \psi \rangle|^2 \approx \frac{1}{\ell} \exp \left(-\frac{2|m - m_0|}{\ell} \right), \quad (28)$$

where m labels the eigenstates of the momentum operator \hat{I} , such that $\hat{I}|m\rangle = m|m\rangle$, and m_0 is the initial momentum. The

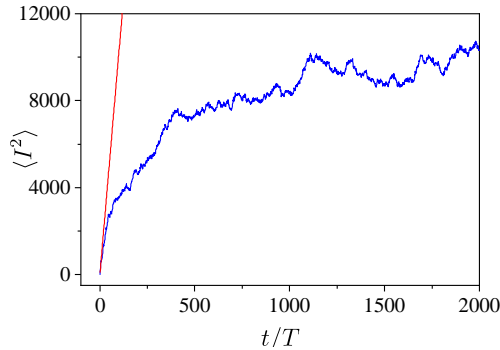


Fig. 2 Quantum localization (blue curve) of classical diffusion (red curve) in the kicked-rotor model. Both classical and quantum evolutions are computed using the parameter values $T = 0.25$ and $k = 20$, corresponding to an effective Planck constant of $\hbar_{\text{eff}} = 0.25$. The classical dynamics are obtained by iterating the Chirikov standard map, starting at time $t = 0$ with an ensemble of 10^6 initial state sampled from Gaussian distribution with variance $\sqrt{\hbar}$ centered at $(0, 0)$. The quantum evolution is simulated by iterating the quantum kicked-rotor map, initialized with a minimum-uncertainty Gaussian wave packet of width $\Delta I = \Delta\theta = \sqrt{\hbar}$, also centered at $(0, 0)$.

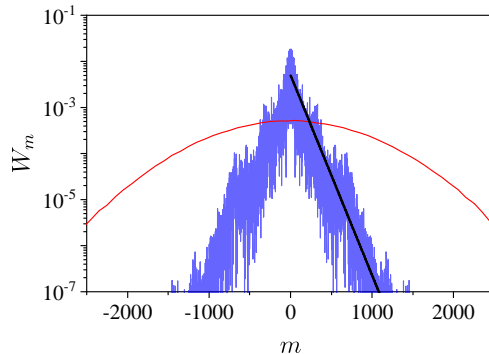


Fig. 3 Classical vs. quantum momentum distributions in the kicked rotor. Classical (red curve) and quantum (blue curve) probability distributions over the momentum basis are shown for the kicked-rotor model at time $t = 3000 \gg t^* \sim D_m \approx k^2/2 \sim 2 \times 10^2$. The dashed curve represents the classical Gaussian distribution, while the solid curve exhibits exponential localization in the quantum case. The straight line corresponds to the theoretical prediction given by Eq. (28), with localization length $\ell = D_m$. Parameter values and initial conditions are identical to those used in Fig. 2.

parameter ℓ , known as the localization length, characterizes the width of the localized momentum distribution.

An estimate of the relaxation time t^* and the localization length ℓ can be obtained through the following argument [27]. During the initial stages of the evolution, the quantum dynamics closely follow classical diffusion. As a result, the number of unperturbed energy levels significantly involved in the dynamics increases with time according to $\Delta m(t) \approx \sqrt{D_m t}$, where $D_m \approx k^2/2$ is the classical diffusion coefficient, measured in terms of the number of momentum eigenstates. Since the number of involved levels grows diffusively, as \sqrt{t} , and because the Heisenberg uncertainty principle limits energy resolution to $\Delta E \sim 1/t$, the discreteness of the spectrum eventually becomes dynamically relevant. This is the fundamental reason why localization occurs.

The localization length ℓ can be estimated as follows. The localized quantum wave packet has significant amplitude over approximately ℓ basis states—both in the basis of momentum eigenstates and in the eigenbasis of the Floquet operator \hat{U} , which governs the time evolution via $|\bar{\psi}\rangle = \hat{U}|\psi\rangle$. Since \hat{U} is unitary, its eigenvalues can be written in the form $\exp(i\epsilon_i)$, where the so-called quasi-energies ϵ_i lie in the interval $[0, 2\pi)$. The mean level spacing between quasi-energy eigenstates that significantly contribute to the dynamics is thus approximately $\Delta E \approx 2\pi/\ell$. According to the energy-time uncertainty principle, the minimum time required to resolve this spacing is given by the Heisenberg time:

$$t^* \approx \frac{1}{\Delta E} \approx \ell. \quad (29)$$

This equation defines the break time, after which quantum features become dominant and the classical diffusive behavior is suppressed. Up to time t^* , diffusion involves a number of levels estimated as

$$\langle (\Delta m)^2 \rangle \approx D_m t^* \approx \ell^2. \quad (30)$$

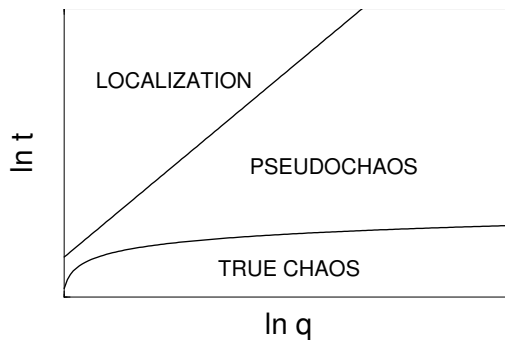


Fig. 4 Schematic representation of the characteristic time scales in the kicked-rotor model as a function of the quasi-classical parameter $q = 1/\hbar_{\text{eff}}$. The lower curve represents the Ehrenfest time scale $t_E \sim \frac{1}{\lambda} \ln q$, while the upper curve shows the Heisenberg (or localization) time scale $t^* \sim q^2$. In the semiclassical limit $\hbar_{\text{eff}} \rightarrow 0$ (i.e., $q \rightarrow \infty$), both time scales diverge, in agreement with the correspondence principle.

Combining Eqs. (29) and (30), we obtain the key relation

$$t^* \approx \ell \approx D_m. \quad (31)$$

Thus, the quantum localization length ℓ for the average probability distribution is approximately equal to the classical diffusion coefficient. In accordance with the correspondence principle, this time scale diverges in the semiclassical limit:

$$t^* \sim \frac{k^2}{2} \sim \frac{1}{\hbar_{\text{eff}}^2}, \quad (32)$$

where the final scaling follows from the relation $\hbar_{\text{eff}} = T \sim 1/k$ at fixed K . Moreover, $t^* \gg t_E$, where t_E is the Ehrenfest time. This implies that classical-like diffusion can persist well beyond the Ehrenfest time, even in the absence of exponential instability.

The concept of characteristic time scales in quantum dynamics reconciles the absence of dynamical chaos (as defined in ergodic theory) in quantum mechanics with the correspondence principle. The crucial point is that the following two limits do not commute:

$$\lim_{|t| \rightarrow \infty} \lim_{\hbar_{\text{eff}} \rightarrow 0} \neq \lim_{\hbar_{\text{eff}} \rightarrow 0} \lim_{|t| \rightarrow \infty}. \quad (33)$$

While the left-hand side leads to classical chaos, the right-hand side results in an essentially quantum behavior with no chaos. Both true chaos—characterized by exponential sensitivity to initial conditions—and pseudochaos—associated with quantum diffusion—are transient phenomena that manifest only over finite time intervals (see Fig. 4). The characteristic time scales over which these classical-like behaviors take place in the quantum dynamics of classically chaotic systems diverge in the semiclassical limit $\hbar_{\text{eff}} \rightarrow 0$, in agreement with the correspondence principle.

2.4 Kicked rotor and Anderson localization

Dynamical localization exhibits deep analogies with Anderson localization, which describes the suppression of electronic transport in disordered solids [28]. In a random potential, a classical particle performs a random walk and eventually diffuses over a distance whose mean square grows linearly with time. It was first realized by Anderson that a quantum particle does not necessarily behave in this manner; depending on dimensionality and energy, it may instead remain localized indefinitely in the vicinity of its initial position. In the context of Anderson localization, particular attention is given to so-called tight-binding models, which arise from the lattice discretization of the Schrödinger equation. These models play a fundamental role in the study of transport properties in solids, particularly at low temperatures, where the electron wave function becomes highly sensitive to local impurities and imperfections in the crystal lattice.

In one dimension, the Anderson model is described by the eigenvalue equation

$$(Hu)_n = W_n u_n + t(u_{n-1} + u_{n+1}) = E u_n, \quad (34)$$

where u_n is the amplitude of the electronic wave function at lattice site n , t denotes the hopping amplitude (i.e., kinetic energy term) between nearest-neighbor sites, and W_n are random on-site energies. These random variables are assumed to be independently distributed. A common choice is to take W_n uniformly distributed over the interval $[-W/2, W/2]$, where W sets the disorder strength. A remarkable property of the one-dimensional Anderson model is that all eigenfunctions are exponentially localized, regardless of how small the disorder strength W is (see, e.g., Ref. [29]). For a given eigenstate, the

wave function decays as:

$$u_n \propto \exp\left(-\frac{|n - n_0|}{\ell}\right), \quad (35)$$

where ℓ is the localization length and n_0 is the center of localization (we assume the lattice size $N \gg \ell$).

Localization arises as a combined result of quantum tunneling and interference effects. A qualitative argument can be formulated as follows: Consider a disordered potential as a sequence of potential steps with varying heights, separated by regions of zero potential. If the electron is initially located in the n -th region, it has a probability $p_t(n)$ of being transmitted to the $(n + 1)$ -th region, and a probability $p_r(n)$ of being reflected by the potential barrier, such that $p_t(n) + p_r(n) = 1$. This process bears similarities to a classical random walk in configuration space, leading to diffusion. However, in quantum mechanics, interference effects of the wave packet play a crucial role. Specifically, the average transmission probability through two consecutive barriers is smaller than the product of the individual transmission probabilities due to destructive interference. As a consequence, the total transmission probability through a large number of potential steps $n \gg 1$ decays exponentially with n , indicating that the electron becomes localized. This phenomenon—known as Anderson localization—arises from the interplay between quantum coherence and disorder.

In both the kicked rotor and the Anderson model, quantum interference effects inhibit unbounded diffusion—occurring in momentum space in the former, and in real space in the latter. This analogy can be formalized through a transformation that maps the quantum kicked rotor onto a disordered tight-binding model [30, 31]. Consider the eigenvalue equation for the Floquet operator of the kicked rotor:

$$\hat{U}|\psi\rangle = e^{-i\hat{H}_0 T} e^{-i\hat{V}}|\psi\rangle = e^{-i\varepsilon T}|\psi\rangle, \quad (36)$$

where $\hat{H}_0 = \hat{I}^2/2$ is the unperturbed Hamiltonian, and the kicking potential is given by $V(\theta) = k \cos \theta$. To proceed, we define two operators \hat{W} and \hat{t} through the following Cayley transformations:

$$e^{-i(\hat{H}_0 - \varepsilon)T} = \frac{1 + i\hat{W}}{1 - i\hat{W}}, \quad e^{-i\hat{V}} = \frac{1 + i\hat{t}}{1 - i\hat{t}}, \quad (37)$$

which allows us to recast the Floquet eigenvalue problem into a more tractable algebraic form. Introducing the transformed state:

$$|\phi\rangle = (1 - i\hat{t})^{-1}|\psi\rangle, \quad (38)$$

we find that the eigenvalue equation reduces to:

$$(\hat{W} + \hat{t})|\phi\rangle = 0. \quad (39)$$

We now expand the state $|\phi\rangle$ over the momentum eigenbasis $\{|m\rangle\}$:

$$|\phi\rangle = \sum_{m=-\infty}^{+\infty} u_m |m\rangle, \quad \langle \theta | m \rangle = \frac{1}{\sqrt{2\pi}} e^{im\theta}. \quad (40)$$

Substituting this expansion into the transformed eigenvalue equation $(\hat{W} + \hat{t})|\phi\rangle = 0$, we obtain a tight-binding-like recursion relation:

$$W_n u_n + \sum_{\substack{l=-\infty \\ (l \neq 0)}}^{+\infty} t_l u_{n+l} = E u_n, \quad (41)$$

where the site energies W_n and hopping amplitudes t_l are given by:

$$W_n = \tan\left(\frac{1}{2}\left(\varepsilon T - \frac{1}{2}n^2 T\right)\right), \quad t_l = -\frac{1}{2\pi} \int_0^{2\pi} d\theta e^{il\theta} \tan\left(\frac{V(\theta)}{2}\right), \quad (42)$$

with $E_{\pm} = -t_0$. The tight-binding model (41) describes the motion of an electron in a lattice with lattice site n , site energies W_n and hopping amplitudes t_l . In contrast to the standard Anderson model (34), the hopping terms here are not restricted to nearest-neighbour sites.

It is important to note that, unlike in the Anderson model, the site energies W_n are not drawn from a random distribution but are instead determined by the system's dynamics. Nevertheless, if the ratio $T/(4\pi)$ is irrational, the sequence $\{W_n\}$ becomes effectively pseudo-random, leading to Anderson-like localization. This correspondence has been confirmed by several numerical studies showing exponential localization of the eigenfunctions when T is an irrational multiple of 4π . On the other hand, when $T/(4\pi)$ is a rational number, the site energies W_n become periodic. In this case, the eigenfunctions are extended Bloch waves, and the particle propagates freely through the lattice. In the context of the kicked rotor, this corresponds to the quantum resonances discussed earlier.

It should be emphasized that, in the dynamical case:

- (i) Localization occurs in momentum space rather than in configuration space, and is associated with the quasi-energy

eigenfunctions of the Floquet operator;

- (ii) No external randomness is introduced; the kicking potential is strictly periodic in time.

For these reasons, the localization phenomenon arising from quantum interference in classically chaotic systems is referred to as dynamical localization, to distinguish it from Anderson localization, which originates from static disorder in the Hamiltonian ⁴.

2.5 Experimental realizations: a brief overview

2.5.1 The hydrogen atom in a microwave field

One of the most significant cases where classical and quantum chaos were directly confronted is the explanation of the experiments on the microwave ionization of highly excited hydrogen atoms [32, 33]. In these experiments, hydrogen atoms were prepared in very elongated Rydberg states with a high principal quantum number $n_0 \approx 63\text{--}69$ and injected into a microwave cavity. The ionization rate was then measured as a function of the microwave field intensity. The applied microwave frequency was $\omega = 9.9\text{ GHz}$, corresponding to a photon energy much smaller than the ionization energy of level $n = 66$, and even lower than the energy required for a single-photon transition between adjacent levels (e.g., from $n = 66$ to $n = 67$). Surprisingly, efficient ionization was observed when the electric field amplitude exceeded a threshold value $\varepsilon \approx 20\text{ V/cm}$, which is significantly lower than the static field required for Stark ionization. The threshold behavior was explained within the framework of classical dynamics, as the critical field strength corresponding to the onset of chaotic diffusion in the classical action variable n [34, 35, 36]. However, the hydrogen atom remains a fundamentally quantum object, and it is possible to identify parameter regimes—analogue to those of the quantum kicked rotor—where classical chaotic diffusion is suppressed by quantum interference. This leads to the phenomenon of quantum localization, where ionization is effectively inhibited despite the presence of classically chaotic dynamics.

The Hamiltonian for a hydrogen atom interacting with a time-periodic, linearly polarized electric field, in the dipole approximation, is given by:

$$H = \frac{p^2}{2} - \frac{1}{r} + \varepsilon z \cos(\omega t), \quad (43)$$

where ε and ω are the amplitude and the frequency of the electric field, respectively, which is assumed to be directed along the z -axis ⁵. When the electron occupies a state that is highly extended along the direction of the electric field, the one-dimensional model becomes a good approximation of the full three-dimensional motion. This model is described by the Hamiltonian:

$$H_{1D} = \frac{p^2}{2} - \frac{1}{z} + \varepsilon z \cos(\omega t), \quad z > 0. \quad (44)$$

The unperturbed Hamiltonian

$$H_{1D}^{(0)} = \frac{p^2}{2} - \frac{1}{z} \quad (45)$$

describes both bound motion (for energies $E < 0$) and unbound motion (for $E > 0$). Since we are primarily interested in the dynamics preceding ionization, we restrict ourselves to negative energies and introduce action-angle variables (n, θ) , leading to the Hamiltonian:

$$H_{1D} = -\frac{1}{2n^2} + \varepsilon z(n, \theta) \cos(\omega t). \quad (46)$$

It is important to note that the classical dynamics depends only on the rescaled parameters $\varepsilon_0 \equiv \varepsilon n_0^4$ and $\omega_0 \equiv \omega n_0^3$, where n_0 is the initial value of the action variable (corresponding, in the quantum case, to the principal quantum number of the initial state). To demonstrate this scaling behavior, we perform the following variable transformations:

$$z \rightarrow \frac{z}{n_0^2}, \quad t \rightarrow \frac{t}{n_0^3}, \quad \varepsilon \rightarrow n_0^4 \varepsilon, \quad \omega \rightarrow n_0^3 \omega. \quad (47)$$

Under these transformations, the momentum scales as $p = \frac{dz}{dt} \rightarrow n_0 p$, and the Hamiltonian transforms as $H_{1D} \rightarrow n_0^2 H_{1D}$. Since the Hamiltonian is only multiplied by a constant factor, the equations of motion remain unchanged; only the size of the trajectories is rescaled. If the initial unperturbed energy is $E = -\frac{1}{2n_0^2}$, then the transformation (47) maps this to the energy of the first Bohr level: $E \rightarrow n_0^2 E = -\frac{1}{2}$. We also observe that the parameters ε_0 and ω_0 represent, respectively, the ratio of the field strength ε to the characteristic Coulomb field strength $\varepsilon_C = z^{-2} \sim n_0^{-4}$, and the ratio of the driving frequency ω to the unperturbed Kepler orbital frequency $\omega_K = n_0^{-3}$. Finally, the rescaled time corresponds to the number of unperturbed Kepler

⁴We do not address here the question of how random the sequence W_n must be for Anderson localization to occur. This issue is related to the number-theoretic properties of T .

⁵Note that we use atomic units, where fundamental constants are set to unity: the electron mass $m = 1$, the elementary charge $e = 1$, and the reduced Planck constant $\hbar = 1$.

periods (up to a factor of 2π : $t/n_0^3 = 2\pi t/T_K$, with $T_K = 2\pi n_0^3$).

Scaling (47) is not valid in quantum mechanics. Indeed, the canonical commutation relation is modified under such scaling: $[z, p] \rightarrow [n_0^{-2}z, n_0 p] = i n_0^{-1}$. Therefore, in quantum mechanics an additional parameter appears, which is absent in classical mechanics: the effective Planck constant, $\hbar_{\text{eff}} = \frac{1}{n_0}$. The classical limit corresponds to $\hbar_{\text{eff}} \rightarrow 0$, i.e., $n_0 \rightarrow \infty$, while keeping the rescaled parameters ε_0 and ω_0 constant.

If the field frequency exceeds the electron frequency, $\omega_0 > 1$, it can be shown [11] that the dynamics of system (46) can be approximately described over one Kepler period by a discrete-time map, the so-called Kepler map:

$$\begin{cases} \bar{N} = N + k \sin \phi, \\ \bar{\phi} = \phi + \frac{\pi}{\sqrt{2\omega}} (-\bar{N})^{-3/2}, \end{cases} \quad (48)$$

where $N = E/\omega$, ϕ is the field phase at perihelion, and the perturbation parameter is given by

$$k \approx \frac{2.6 \varepsilon}{\omega^{5/3}}. \quad (49)$$

We obtain a map description because the external field exerts its dominant perturbing effect on the electron's free Keplerian motion primarily when the electron passes near the perihelion. This behavior originates from the Coulomb singularity and results in a kick-like action of the external perturbation. Note that the Kepler map is only defined for states with $N < 0$, i.e., bound states. If an iteration of the map leads to $\bar{N} > 0$, then $E > 0$ and the electron is considered ionized. By linearizing the second equation of (48) around the initial value $N_0 = -\frac{1}{2n_0^2\omega}$, the Kepler map reduces to the standard map:

$$\begin{cases} \bar{N}_\phi = N_\phi + k \sin \phi, \\ \bar{\phi} = \phi + T N_\phi, \end{cases} \quad (50)$$

where $N_\phi = N - N_0$ (interpreted in the quantum case as the number of photons absorbed) and $T = 6\pi\omega^2 n_0^5$ ⁶.

As discussed in Sec. 2.1, the transition to classical chaos occurs when $K = kT \approx 1$, leading to the classical chaos border:

$$\varepsilon_c \approx \frac{1}{49 n_0^5 \omega^{1/3}}, \quad (51)$$

or in terms of rescaled units:

$$\varepsilon_{0c} \approx \frac{1}{49 \omega_0^{1/3}}. \quad (52)$$

On the quantum side, drawing from the kicked-rotor analogy, quantum localization is expected over a length (measured in number of photons):

$$\ell_\phi \approx \frac{k^2}{2} \approx \frac{3.3 \varepsilon^2}{\omega^{10/3}}. \quad (53)$$

The ionization process is thus governed by two characteristic scales:

- (i) the localization length ℓ_ϕ , and
- (ii) the "sample size" N_I , i.e., the number of photons required to reach the continuum from the initial state n_0 ,

$$N_I = \frac{1}{2n_0^2\omega}. \quad (54)$$

If $\ell_\phi \ll N_I$, quantum localization prevents ionization. Conversely, if $\ell_\phi > N_I$, chaotic diffusion proceeds until ionization. The quantum delocalization border is obtained by setting $\ell_\phi = N_I$, which yields:

$$\varepsilon_q \approx 0.4 \frac{\omega^{7/6}}{n_0}. \quad (55)$$

In order to observe chaotic ionization, the condition $\varepsilon > \varepsilon_q$ must be satisfied.

A comparison between localization theory and experimental data [12] is shown in Fig. 5. The empty circles represent the experimentally observed threshold values of the microwave peak intensity required to ionize 10% of the atoms⁷. The dotted curve shows the classical chaos border, while the dashed curve represents the prediction of the localization theory for 10% ionization. The filled circles indicate numerical results obtained from the integration of the quantized Kepler map. The agreement between experimental data and the numerical results is quite remarkable, especially considering that the Kepler map provides only an approximate description of the true quantum dynamics. Furthermore, the localization theory successfully captures the average behavior of the ionization threshold.

⁶An irrelevant constant phase shift has been omitted in the second equation.

⁷This threshold corresponds to a fixed ionization probability and serves as a meaningful indicator for comparing theory and experiment.

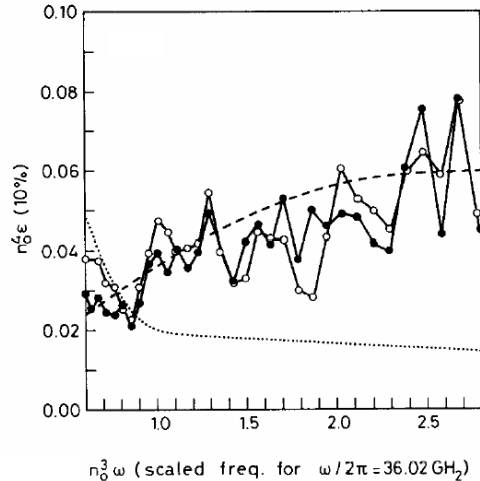


Fig. 5 Scaled 10% ionization threshold field as a function of the rescaled frequency, from experimental data (empty circles, taken from [12]) and from numerical integration of the quantum Kepler map (filled circles). The dashed curve shows the quantum theoretical prediction based on localization theory, while the dotted curve represents the classical chaos border. Figure adapted from [37].

As shown in Fig. 5, both the numerical and experimental data exhibit noticeable deviations from the average theoretical prediction. These fluctuations are analogous to the conductance fluctuations observed in finite solid-state sample [37]. In the case of microwave ionization of hydrogen atoms, the system effectively forms a finite “photonic lattice,” since only a finite number of photons is required to ionize the atom. However, while in solid-state systems—typically modeled by the Anderson Hamiltonian—such fluctuations arise from the static randomness of the potential landscape, in the hydrogen atom they originate from the underlying dynamical chaos of the classical system.

2.5.2 Cold atoms in optical lattices

In this experimental implementation of the quantum kicked rotor model [38, 39], neutral sodium atoms were trapped and cooled using a magneto-optical trap. Then, the atoms were released from the trap and allowed to interact with a flashed optical lattice.

The dynamics is modeled in terms of two-level atoms with transition frequency ω_0 , interacting with a pulsed standing wave of linearly polarized, near-resonant light of frequency ω_L . For sufficiently large detuning $\Delta = \omega_0 - \omega_L$ (relative to the natural linewidth), the excited-state amplitude can be adiabatically eliminated [40]. The atom can then be treated as a point particle, whose center-of-mass motion is described by a kicked-rotor-like Hamiltonian:

$$H = \frac{P^2}{2M} + V_0 \cos(2k_L x) \sum_n F(\tau - nT), \quad (56)$$

where $V_0 = \hbar\Omega^2/8\Delta$, k_L is the wave number of the light, $\Omega = 2\mu E_0/\hbar$ is the resonant Rabi frequency, μ is the atomic dipole moment, E_0 is the electric field amplitude, $F(\tau)$ represents a pulse centered at $t = 0$ with duration τ_p , and T is the period of the standing wave pulses⁸.

Using the rescaled units $\phi = 2k_L x$, $p = (2k_L T/M)P$, and $t = \tau/T$, one can write the dimensionless Hamiltonian:

$$\tilde{H} = \frac{p^2}{2} + k \cos(\phi) \sum_n f(t - n), \quad (57)$$

$f(r)$ is a dimensionless pulse function of unit amplitude and duration τ_p/T , k is the dimensionless kick strength given by $k = (8V_0/\hbar)\omega_r T^2$, with $\omega_r = \hbar k_L^2/2M$ being the recoil frequency, and the rescaled Hamiltonian \tilde{H} is related to the original Hamiltonian H via $\tilde{H} = (4k_L^2 T^2/M)H$. In the quantized version of the model, ϕ and p are conjugate variables satisfying the commutation relation $[\phi, p] = i\hbar_{\text{eff}}$, where the effective Planck constant is defined as $\hbar_{\text{eff}} = 8\omega_r T$.

Figure 6 provides direct evidence of dynamical localization: the mean energy initially grows linearly with time and then saturates. The inset shows the localized, exponential profile of the momentum distribution for the evolved cold atomic cloud.

⁸In Ref. [38] a train of Gaussian pulses was used.

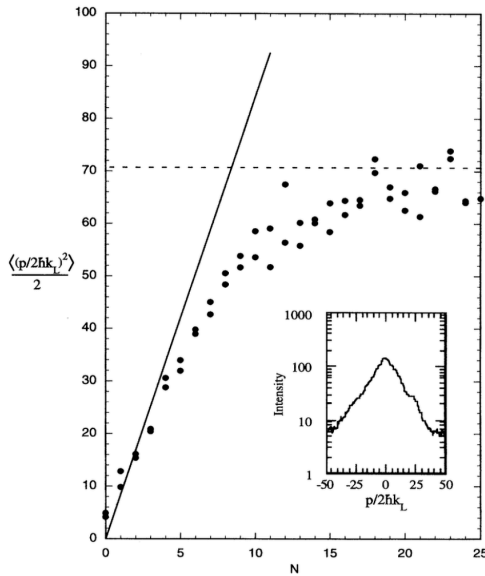


Fig. 6 Experimental observation of dynamical localization. Solid symbols show the saturation of the mean energy as a function of time N (measured in number of kicks). The dashed line indicates the expected saturation energy from quantum localization theory, while the solid line represents the classical quasi-linear diffusive growth. The inset shows the experimentally measured momentum distribution, consistent with exponential localization over a length $\ell = k^2/2 \approx 8.3$. Figure taken from [38].

2.5.3 Variants of kicked rotor

Variants of the kicked rotor model allow for the experimental investigation of relevant physical phenomena. In this section, we focus on the localization–delocalization transition in a generalized kicked rotor model, which is analogous to the three-dimensional Anderson model, as well as on quantum computing of a kicked map using actual quantum hardware.

The Anderson metal–insulator transition is a key phenomenon in the study of quantum disordered systems. An insulator is characterized by localized states, whereas a metallic phase generally exhibits diffusive transport, associated with delocalized states. While all states are localized in one and two dimensions, the Anderson model predicts a metal–insulator transition in three dimensions, driven by increasing either the disorder strength or the energy [41]. As discussed in Sec. 2.4, there exists a mapping between the kicked rotor and a one-dimensional tight-binding model with pseudo-random disorder. A generalized, quasiperiodic kicked rotor model,

$$H = \frac{p^2}{2} + K \cos x [1 + \epsilon \cos(\omega_2 t) \cos(\omega_3 t)] \sum_n \delta(t - n), \quad (58)$$

with the frequencies ω_2 and ω_3 incommensurate with each other, and also with the kicking frequency, is substantially analogous to the three-dimensional Anderson model [42]. In this model, a transition from an insulating to a metallic phase—that is, from localized to delocalized momentum distributions—can be induced by increasing either the kicking strength K or the amplitude modulation ϵ . These theoretical predictions have been confirmed experimentally using cold cesium atoms exposed to a pulsed laser standing wave [43], see Fig. 7.

While the experiments described in Sec. 2.5.2 are quantum simulations of the kicked rotor model, the dynamics of the same model is amenable also to quantum computing, that is, it can be numerically evaluated using a universal quantum computer. In that case the operators \hat{U}_T and \hat{U}_k in (19) can be decomposed on a universal set of quantum gates (such as single-qubit and CNOT gates [44]). The operators \hat{U}_T and \hat{U}_k are diagonal in the action and angle basis, respectively, and one can go from one basis to the other by means of the Fourier transform, which can be implemented efficiently in a quantum computer [44]. For a kicked rotor with N levels, the Fourier transform requires $O((\log_2 N)^2)$ quantum gates, while $O((\log_2 N)^3)$ quantum gates are required to simulate one map step [45], while the best known classical algorithm, based on the fast Fourier transform for the changes of basis, requires $O(N \log_2 N)$ operations. Therefore, the quantum algorithm which computes the dynamics of the quantum kicked rotor is exponentially faster than any known classical algorithm. Note that efficient implementation of the operator \hat{U}_k necessitates the introduction of auxiliary qubits. Even more efficient is the quantum computation of the dynamics of the quantum sawtooth map, where a particle moving on a circle is periodically kicked as in (3), but with a potential $V(\theta) = -k(\theta - \pi)^2/2$ ⁹. In this case there is no need of auxiliary qubits and the complexity

⁹This map is referred to as the sawtooth map since the force $F(\theta) = -\frac{dV(\theta)}{d\theta} = k(\theta - \pi)$ has a sawtooth shape, featuring a discontinuity at $\theta = 0$.

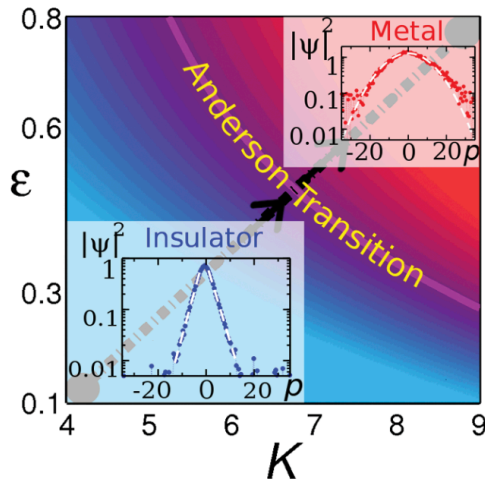


Fig. 7 Phase diagram of the quasiperiodic kicked rotor obtained from numerical simulations. The localized (insulating) region is shown in blue, while the diffusive (metallic) region appears in red. Experimental parameters are varied along the diagonal dash-dotted line. Insets display the experimentally observed momentum distributions: an exponentially localized profile in the insulating phase and a Gaussian distribution in the diffusive (metallic) phase. Figure taken from [43].

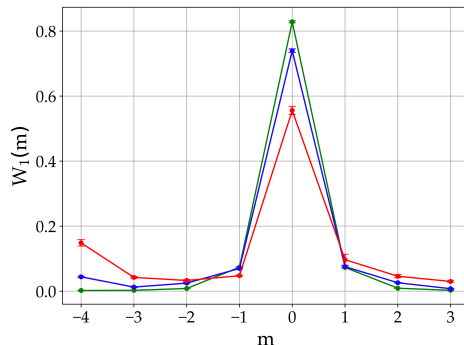


Fig. 8 Dynamical localization in the quantum sawtooth map with $n = 3$ qubits. The probability distribution W_1 (after one pulse) is obtained from an IBM quantum processor (red) are compared with the Qiskit simulator (blue) and the ideal noiseless simulation (green). Figure adapted from [49].

of the quantum algorithm scales as $O((\log_2 N)^2)$ [46, 47].

Dynamical localization in the quantum sawtooth map has been observed experimentally on NMR quantum processors [48] and, more recently, using a freely available IBM quantum processor with three superconducting qubits, accessed remotely through cloud-based quantum programming [49]. In the example shown in Fig. 8, the initial condition is sharply peaked in action space, with $\psi_0(m) = \delta_{m,m_0}$ ($m_0 = 0$). The kick strength is $k = 0.273 < 1$, so the distribution becomes localized after a single map step. However, $K = kT = 1.5$ corresponds to a regime of diffusive, chaotic behavior in the underlying classical dynamics. The figure compares the ideal (noiseless) probability distribution after $t = 1$ map step with the results obtained from a real quantum device and from the Qiskit simulator (provided by IBM), which models several relevant noise sources, including dephasing, relaxation, and readout errors. The results show that the quantum hardware exhibits a localization peak that arises from quantum interference. This is notable because the quantum algorithm involves a forward–backward quantum Fourier transform, effectively exploring the full Hilbert space of the quantum register via a complex, multi-path interferometer. This process leads to wavefunction localization—an inherently fragile quantum phenomenon that is highly sensitive to noise. However, the observed peak height in the hardware results is significantly lower than both the ideal noiseless prediction and the outcome from the Qiskit simulator¹⁰.

¹⁰This indicates the existence of noise channels not properly taken into account by the simulator, showing that correctly modeling error sources in a quantum computer is, in itself, a complex problem.

3 Selected advancements

3.1 Pseudoclassical theory of near-resonance dynamics

Although quantum resonances are usually regarded as a purely quantum effect, it turns out that in the near-resonant regime their dynamics can be captured by a pseudoclassical (or ε -classical) theory [50, 51]. The pseudoclassical approach is inspired by a rescaling usually done for the standard semiclassical limit of the quantum kicked rotor, which, as we discussed before, is obtained by simultaneously taking the kick period $T \rightarrow 0$ and the kick strength $k \rightarrow \infty$, while keeping their product fixed. A similar variable rescaling can be applied for kick periods T that are not small – and thus far from the standard classical limit – but lie within the near-resonance region. In what follows, we will first focus on the low-order-resonance cases – principal resonance and anti-resonance cases, which correspond to $T = 2\pi l$ with even and odd l , respectively –, then show applications to the double kicked rotor system, and finally present recent extensions to high-order resonances.

For the low-order resonance cases, we consider the situation where the kicking period is slightly detuned from the resonance condition, i.e., $T = 2\pi l + \delta$, where δ is an irrational multiple of π . For simplicity, we assume $\delta > 0$ throughout. Then the Floquet operator reads

$$\hat{U} = \exp(-i\pi l \hat{I}^2) \exp\left(-i\frac{\delta}{2} \hat{I}^2\right) \exp(-ik \cos \hat{\theta}). \quad (59)$$

Using the identity $\exp(-i\pi l \hat{I}^2) = \exp(-i\pi l \hat{I})$, the above equation can be expressed as

$$\hat{U} = \exp(-i\pi l \hat{I}) \exp\left(-i\frac{\delta}{2} \hat{I}^2\right) \exp(-ik \cos \hat{\theta}). \quad (60)$$

In analogy with the semiclassical limit, we now consider taking the limit $\delta \rightarrow 0$ and $k \rightarrow \infty$, while keeping the product $k\delta \equiv K$ fixed. Note that if we define the rescaled momentum operator $\hat{J} = \delta \hat{I}$, it is straightforward to verify the commutation relation $[\hat{J}, \hat{\theta}] = -i\delta$, which indicates that δ plays a role analogous to the Planck constant. Consequently, equation (60) formally defines the quantized version of the Hamiltonian

$$H(\theta, J; t) = \frac{J^2}{2} + \pi l J + K \cos \theta \sum_{n=-\infty}^{+\infty} \delta(t - n). \quad (61)$$

The corresponding stroboscopic classical map is given by

$$\begin{cases} \bar{J} = J + K \sin \theta, \\ \bar{\theta} = \theta + \bar{J} + \pi l. \end{cases} \quad (62)$$

Thus, the pseudoclassical map offers a classical representation of the near-resonant quantum dynamics, with the parameter δ effectively playing the role of a Planck-like constant. This approach bridges the quantum and classical descriptions, enabling both insightful and tractable analysis of kicked rotor systems in the vicinity of resonance [50, 51, 52, 53].

A particularly significant application of pseudoclassical theory is its ability to explain the long-lived exponential and superballistic wavepacket diffusion observed in double-kicked rotor systems [54]. In this setup, the rotor experiences two kicks within each period T , and the corresponding Floquet operator is given by

$$\hat{U} = \exp\left(-i\frac{(T - T_0)}{2} \hat{I}^2\right) \exp(-ik \cos \hat{\theta}) \exp\left(-i\frac{T_0}{2} \hat{I}^2\right) \exp(-ik \cos \hat{\theta}). \quad (63)$$

When $T = 2T_0$, this becomes equivalent to viewing a single-kicked rotor system with an effective period of $2T_0$. Interestingly, dynamics emerge when the kicking period T is at a principal resonance and T_0 is slightly detuned from specific resonant parameters. Under these conditions, long-time exponential wave-packet spreading can be observed for certain special initial states. A concrete example is given by choosing $T = 4\pi$ and $T_0 = 2\pi + \delta$, where δ is small. For this set of parameters, the Floquet operator in Eq. (63) can be seen as the quantized version of the classical map

$$\begin{cases} J' = J + K \sin \theta, \\ \theta' = \theta + \pi + J + K \sin \theta, \\ \bar{J} = J' + K \sin \theta', \\ \bar{\theta} = \theta' - \pi - J' - K \sin \theta'. \end{cases} \quad (64)$$

Remarkably, this map can be recognized as a variant of the kicked-Harper model, which processes nearly straight stable and unstable manifolds in the near-integrable regime [55, 56]. To see this we perform a change of variables from the classical pair (J, θ) to $(J + \theta, \theta)$, under which the map in Eq. (64) transforms into

$$\begin{cases} \bar{J} + \bar{\theta} = (J + \theta) + K \sin \theta, \\ \bar{\theta} = \theta + K \sin(\bar{J} + \bar{\theta}), \end{cases} \quad (65)$$

which is precisely the classical map of the kicked-Harper model. Through linear stability analysis, it can be shown that this

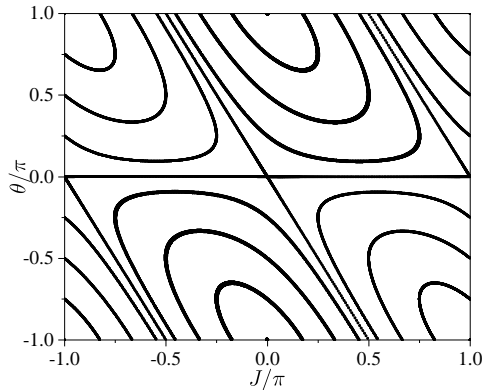


Fig. 9 Phasespace portrait of the pseudoclassical map of the double-kicked rotor. Classical kicking strength $K = 0.005$. (Adapted from [54].)

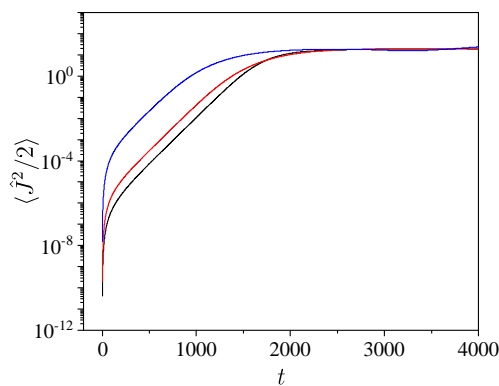


Fig. 10 Long-lasting exponential quantum spreading in the double kicked rotor. The blue, red, and black lines correspond to $\delta = 10^{-1}, 10^{-2}, 10^{-3}$, respectively, with $K = 0.005$ fixed.

model possesses unstable fixed points at $(J + \theta, \theta) = (n\pi, m\pi)$, where $m, n \in \mathbb{Z}$ and $m + n$ is even. The Lyapunov exponent at each unstable fixed point is given by $\lambda_{\pm} = \ln[(K^2 + 2 \pm \sqrt{K^2 + 4K})/2]$. In the limit $K \rightarrow 0$, the stable and unstable manifolds of these fixed points form a periodic network, dividing phase space into cells shaped like parallelograms, with two sides parallel to the θ -axis and the other two inclined at an angle of $\arctan 2$ (see Fig. 9). Due to the near-linear structure of these manifolds, classical trajectories in the vicinity of the unstable fixed points can exhibit long-time exponential divergence. This phase-space structure provides a compelling explanation for the observed exponential wavepacket spreading. Consider an initial quantum state $|\psi\rangle = |0\rangle$, an eigenstate of \hat{J} with zero eigenvalue. Classically, this corresponds to an ensemble narrowly distributed along the stable manifold of the unstable fixed point at $(J, \theta) = (0, \pi)$, with an initial width $\Delta J(0) = \delta$. Under time evolution, the pseudoclassical map first drives the ensemble toward the fixed point, then repels it exponentially along the unstable manifold at a rate λ_+ . This exponential momentum growth along the unstable manifold continues until a time t such that $J(t) \sim \pi$ (see Fig. 10). Using the relation $J(t) \sim \Delta J(0) \exp(\lambda_+ t)$, the timescale for exponential spreading can be estimated as $t_{\text{exp}} \sim 1/\lambda_+ \ln(\pi/\delta)$, which shows excellent agreement with numerical results, as shown in [54].

In the above discussion we have restricted ourselves to the kicking potential of the form $k \cos \theta$. If one instead considers other non-KAM singular potentials that satisfy the symmetry $V(\theta) = -V(\theta + \pi)$, for example, $V(\theta) = \frac{2\theta}{\pi} + 1$ for $-\pi \leq \theta < 0$ and $V(\theta) = -\frac{2\theta}{\pi} + 1$ for $0 \leq \theta < \pi$, the wavepacket can exhibit superballistic spreading ($\sim t^3$) which can also be well explained within the pseudoclassical framework. Further details on such systems can be found in [57].

Finally, we turn to the case of high-order resonances [58, 59, 60]. When the neighborhood of such a resonance is considered, the Floquet operator with a small detuning $T = 4\pi r/s + \delta$ takes the form

$$\hat{U} = \exp\left(-i\frac{4\pi r}{s}\hat{I}^2\right) \exp\left(-i\frac{\delta}{2}\hat{I}^2\right) \exp(-ik \cos \hat{\theta}). \quad (66)$$

For the last two terms, applying the same rescaling procedure as in the low-order resonance cases yields a well-defined pseudoclassical limit. However, the first term can no longer be simplified to a single translation operator; instead, it

decomposes into a superposition of multiple translation operators:

$$\exp\left(-i\frac{4\pi r}{s}\hat{p}^2\right) = \sum_{l=0}^{s-1} G_l \exp\left(-i\frac{2\pi r}{s}l\hat{p}\right), \quad (67)$$

where the coefficients G_l are given by a Gaussian sum defined by

$$G_l = \frac{1}{s} \sum_{m=0}^{s-1} \exp\left(-i2\pi\frac{r}{s}m(m-l)\right). \quad (68)$$

It can be proven that when l is odd, all $G_l \neq 0$, whereas if s is even, exactly half of the G_l coefficients vanish. Physically, this implies that the resonant Floquet spectrum splits into s or $s/2$ quasienergy bands; each band is associated with a Bloch phase $\frac{2\pi r}{s}l$. By incorporating this with the last two terms in equation (66), each quasienergy band can be effectively approximated by a local pseudoclassical Hamiltonian,

$$H^{(l)}(J, \theta; t) = \frac{J^2}{2} + \frac{2\pi r}{s}lJ + K \cos \theta \sum_{n=-\infty}^{+\infty} \delta(t-n), \quad (69)$$

and the full quantum dynamics corresponds to a coherent superposition of contributions from different quasienergy bands. It now becomes evident that in the high-order near-resonance regime, a single global pseudoclassical approximation based on one Hamiltonian is generally no longer sufficient. Instead, one must adopt a set of local pseudoclassical descriptions, each associated with a distinct quasienergy band. However, interference between bands can undermine these local approximations and render their predictions unreliable. Consequently, the near-resonant dynamics at high-order resonances cannot be captured by a single classical map alone. Rather, they must be understood as arising from an ensemble of classical maps – each corresponding to a quasienergy band – along with the quantum interference among them. This motivates a formal representation of the pseudoclassical evolution as

$$\mathcal{M}: (J, \theta) \rightarrow \{(J', \theta' + \Delta_j); A_j, j = 1, \dots, \mathcal{N}\}. \quad (70)$$

Here $\mathcal{N} = s$ or $s/2$ denotes the number of quasienergy bands, (J', θ') is obtained from (J, θ) via one-step evolution under Hamiltonian $H^{(l)}(J, \theta; t)$ in Eq. (69), and each A_j is a non-zero Gaussian sum corresponding to the Bloch phase Δ_j . Compared to the low-order case, in which the classical phase space evolution $(J(t), \theta(t))$, alone is sufficient, one must now also track the amplitude and phase information carried by the set $\{A_j\}$ to correctly reconstruct the full quantum dynamics. The relative phases encoded in $\{A_j\}$ are essential for capturing quantum interference effect. In particular, $|A_j|^2$ serves as the weight of the j th classical state $(J', \theta' + \Delta_j)$ when evaluating expectation values of observables. This framework successfully describes quantum dynamics across all resonance orders, as confirmed by numerical simulations in [60]. However, as demonstrated in equation (70), for generic high-order resonances, such framework leads to a rapid proliferation of classical states – typically growing as \mathcal{N}^t , with t number of map iterations, which limits the method's applicability to short or intermediate timescales. Only certain symmetries of the kicking potential can suppress this proliferation, thereby enabling accurate long-time predictions [60].

The pseudoclassical theory has been successfully extended to both non-Hermitian kicked rotor [60] and kicked top systems [61, 62]. In the non-Hermitian kicked rotor, the intrinsic dissipative dynamics effectively suppress the exponential proliferation of classical states, thereby addressing the major challenge of state growth for high-order resonances [60]. In the case of the kicked top system, the pseudoclassical framework accurately predicts wave packet recurrence and offers a comprehensive explanation of the dynamics of entanglement entropy [61]. Moreover, it may lead to promising applications in quantum metrology by enabling enhanced precision through near-resonant dynamics [62].

3.2 Floquet topological phases

Periodic driving has become a foundational technique for engineering topological phases in contemporary condensed matter physics. The kicked rotor, as a paradigmatic Floquet system, exhibits a rich landscape of Floquet topological phases. Particularly intriguing is the resonant regime, where the kicking period matches specific system frequencies, leading to an effective Floquet Hamiltonian that maps onto a tight-binding model in momentum space. This emergent lattice structure enables the realization of topological phases, with internal degrees of freedom playing a pivotal role in their formation. A variety of exotic Floquet topological phases have been theoretically proposed within this framework. In the following, we will first introduce the topological phases arising in the double kicked rotor, as well as its quantized adiabatic transport [63], and subsequently present how the spin-1/2 double kicked rotor can be employed to realize all nontrivial one-dimensional topological phases [64, 65].

To characterize the band topology of the on-resonance double-kicked rotor, we introduce an additional periodic phase parameter $\alpha \in (0, 2\pi]$, which plays a role analogous to that of a synthetic dimension. The Floquet operator is given by

$$\hat{U}(\alpha) = \exp\left(-i\frac{(T-T_0)}{2}\hat{p}^2\right) \exp(-ik \cos \hat{\theta}) \exp\left(-i\frac{T_0}{2}\hat{p}^2\right) \exp(-ik \cos(\hat{\theta} + \alpha)). \quad (71)$$

Here we set $T = 4\pi$ and $T_0 = 2\pi r/s$. Under these conditions, $\hat{U}(\alpha)$ is perfectly periodic in momentum space with a period of s , which allows for the application of Bloch's theorem, and the Floquet eigenvalue problem

$$\hat{U}(\alpha)|\psi_n(\phi, \alpha)\rangle = e^{i\omega_n(\phi, \alpha)}|\psi_n(\phi, \alpha)\rangle \quad (72)$$

defines s Floquet bands $\omega_n(\phi, \alpha)$, where $\phi \in [0, 2\pi)$ is the Bloch phase in momentum space. The eigenstates can be factorized as $|\psi_n(\phi, \alpha)\rangle = \hat{X}(\phi)|u_n(\phi, \alpha)\rangle$, with $\langle m|u_n(\phi, \alpha)\rangle = \langle m + ls|u_n(\phi, \alpha)\rangle$ and $\hat{X}(\phi) \equiv e^{i\phi/s}$. To obtain a reduced representation, we define the projected state $|\bar{u}_n(\phi, \alpha)\rangle = \sum_{m=1}^s |m\rangle\langle m|u_n(\phi, \alpha)\rangle$. It can be easily shown that

$$\hat{U}(\phi, \alpha)|\bar{u}_n(\phi, \alpha)\rangle = e^{i\omega_n(\phi, \alpha)}|\bar{u}_n(\phi, \alpha)\rangle, \quad (73)$$

where $\hat{U}(\phi, \alpha)$ is a $s \times s$ Floquet matrix defined by

$$\langle m|\hat{U}(\phi, \alpha)|m'\rangle = \sum_{l=-\infty}^{\infty} \langle m|\hat{X}^\dagger(\phi)\hat{U}(\alpha)\hat{X}(\phi)|m' + ls\rangle, \quad (74)$$

To characterize the topology of these bands, we consider the two-torus defined by (ϕ, α) . For each band n , the Berry connection is defined as

$$A_{n,\mu}(\phi, \alpha) = i\langle \bar{u}_n(\phi, \alpha)|\partial_\mu|\bar{u}_n(\phi, \alpha)\rangle, \quad \mu \in \{\phi, \alpha\}, \quad (75)$$

and the corresponding Berry curvature is

$$\begin{aligned} B_n(\phi, \alpha) &= \partial_\phi A_{n,\alpha} - \partial_\alpha A_{n,\phi} \\ &= i \left[\left(\frac{\partial}{\partial \phi} \langle \bar{u}_n(\phi, \alpha) | \right) \frac{\partial}{\partial \alpha} |\bar{u}_n(\phi, \alpha)\rangle - \left(\frac{\partial}{\partial \alpha} \langle \bar{u}_n(\phi, \alpha) | \right) \frac{\partial}{\partial \phi} |\bar{u}_n(\phi, \alpha)\rangle \right] \\ &= i \sum_{n'=1, \neq n}^s \left[\left(\frac{\partial}{\partial \phi} \langle \bar{u}_n(\phi, \alpha) | \right) |\bar{u}_{n'}(\phi, \alpha)\rangle \langle \bar{u}_{n'}(\phi, \alpha) | \frac{\partial}{\partial \alpha} |\bar{u}_n(\phi, \alpha)\rangle - \left(\frac{\partial}{\partial \alpha} \langle \bar{u}_n(\phi, \alpha) | \right) |\bar{u}_{n'}(\phi, \alpha)\rangle \langle \bar{u}_{n'}(\phi, \alpha) | \frac{\partial}{\partial \phi} |\bar{u}_n(\phi, \alpha)\rangle \right]. \end{aligned} \quad (76)$$

Physically, $B_n(\phi, \alpha)$ captures the local geometric phase accumulation of the Floquet eigenstates over the parameter space. The topological invariant associated with each band is the Chern number, defined by integrating the Berry curvature over the Brillouin-zone torus:

$$C_n = \frac{1}{2\pi} \int_0^{2\pi} \int_0^{2\pi} B_n(\phi, \alpha) d\phi d\alpha. \quad (77)$$

This integer quantity classifies the global topology of the Floquet bands and is robust against any smooth deformations of system parameters that preserve the quasienergy gaps.

To efficiently compute the Berry curvature in terms of the Floquet operator and its derivatives, we differentiate Eq. (73) with respect to ϕ , and take the inner product with $\langle \bar{u}_{n'}(\phi, \alpha) |$, and rearrange to obtain the Feynman-Hellmann-like relation as

$$\langle \bar{u}_{n'}(\phi, \alpha) | \frac{\partial}{\partial \phi} |\bar{u}_n(\phi, \alpha)\rangle = \frac{\langle \bar{u}_{n'}(\phi, \alpha) | \frac{\partial \hat{U}(\phi, \alpha)}{\partial \phi} | \bar{u}_n(\phi, \alpha)\rangle}{e^{i\omega_n} - e^{i\omega_{n'}}}, \quad (78)$$

which has adjoint given by

$$\left(\frac{\partial}{\partial \phi} \langle \bar{u}_n(\phi, \alpha) | \right) |\bar{u}_{n'}(\phi, \alpha)\rangle = \frac{\langle \bar{u}_n(\phi, \alpha) | \frac{\partial \hat{U}^\dagger(\phi, \alpha)}{\partial \phi} | \bar{u}_{n'}(\phi, \alpha)\rangle}{e^{-i\omega_n} - e^{-i\omega_{n'}}}. \quad (79)$$

Similar expressions also hold for the $\frac{\partial}{\partial \alpha}$ derivative. Substituting Eqs. (78), (79) and the corresponding results for $\frac{\partial}{\partial \alpha}$ into Eq. (76), we obtain a convenient expression for the Berry curvature,

$$B_n(\phi, \alpha) = i \sum_{n'=1, \neq n}^s \left\{ \frac{\langle \bar{u}_n(\phi, \alpha) | \frac{\partial \hat{U}^\dagger}{\partial \phi} | \bar{u}_{n'}(\phi, \alpha)\rangle \langle \bar{u}_{n'}(\phi, \alpha) | \frac{\partial \hat{U}}{\partial \alpha} | \bar{u}_n(\phi, \alpha)\rangle}{|e^{i\omega_n} - e^{i\omega_{n'}}|^2} - \text{c.c.} \right\}. \quad (80)$$

This form is particularly suitable for numerical evaluation, since it only involves the matrix elements of the derivatives of the finite-dimensional operator $\hat{U}(\phi, \alpha)$ ($\hat{U}^\dagger(\phi, \alpha)$) with respect to α (ϕ).

The results of the Chern numbers are shown in Fig. 11. It can be seen that at certain isolated critical values of k the Chern numbers undergo jumps, signaling the presence of topological phase transitions in our double-kicked rotor model. Indeed, the Chern numbers are integer-valued invariants under smooth deformations of the bands and change only discontinuously when bands touch.

A key physical consequence of a non-zero Chern number is the quantization of momentum transport when the synthetic dimension parameter α is slowly cycled. To begin, we construct the initial state as follows:

$$|\Psi_n\rangle = \frac{1}{2\pi} \int_0^{2\pi} d\phi |\psi_n(\phi, \alpha = 0)\rangle, \quad (81)$$

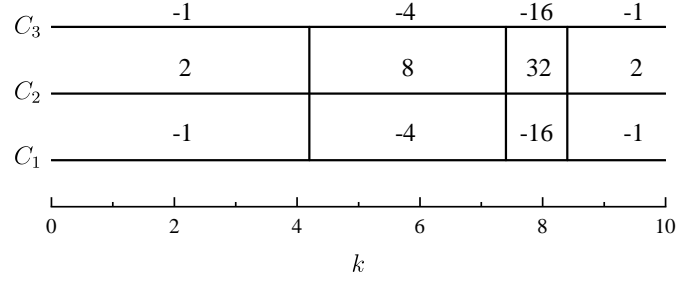


Fig. 11 The Chern numbers of the double kicked rotor for $T_0 = 2\pi/3$. (Adapted from [63].)

which represents an equal-weight superposition of all the Floquet eigenstates of band n . This coherent superposition state, which can be interpreted as a Wannier function in momentum space, uniformly samples all the Bloch eigenstates with different values of ϕ , with a profile localized in the momentum space. Next, we consider an adiabatic evolution of the parameter α via a discretized protocol $\alpha_m = 2\pi d/d_f$ for $(d-1)T \leq t < dT$, such that a full adiabatic cycle is completed at $t = d_f T$. Under the adiabatic approximation, the system remains in a superposition of instantaneous eigenstates of the Floquet operator $\hat{U}(\alpha)$. The time-evolved state at $t = (dT)^-$ is then given by

$$|\Psi_n\rangle = \frac{1}{2\pi} \int_0^{2\pi} d\phi |\psi_n(\phi, \alpha_d)\rangle e^{i\theta(\phi, \alpha_d)}, \quad (82)$$

where $\theta(\phi, \alpha_d)$ denotes the accumulated dynamical and geometric phases.

The central quantity of interest is the expectation value of the momentum operator \hat{I} . We show that the calculation simplifies remarkably, with the final momentum expectation change being purely geometric in origin: We first evaluate the expectation value of the momentum operator \hat{I} in this state. According to the definition, it is expressed as

$$\langle I_d \rangle = \sum_{m=-\infty}^{\infty} m \int_0^{2\pi} d\phi \int_0^{2\pi} d\phi' e^{\frac{im(\phi-\phi')}{s}} \langle m | u_n(\phi, \alpha_d) \rangle \langle u_n(\phi', \alpha_d) | m \rangle \times \frac{1}{4\pi^2} e^{i(\theta(\phi, \alpha_d) - \theta(\phi', \alpha_d))}. \quad (83)$$

Using the identity $m e^{i\frac{m(\phi-\phi')}{s}} = -is \frac{\partial}{\partial \phi} e^{i\frac{m(\phi-\phi')}{s}}$, we integrate by parts and decompose m into $m = ls + m'$, where $l \in \mathbb{Z}$ and $m' \in \{1, 2, \dots, s\}$. This yields:

$$\begin{aligned} \langle I_d \rangle &= \frac{is}{4\pi^2} \sum_{m'=1}^s \sum_{l=-\infty}^{\infty} \int_0^{2\pi} d\phi \int_0^{2\pi} d\phi' e^{\frac{i(m'+ls)(\phi-\phi')}{s}} \frac{\partial}{\partial \phi} \left(\langle m'+ls | u_n(\phi, \alpha_d) \rangle \langle u_n(\phi', \alpha_d) | m'+ls \rangle e^{i(\theta(\phi, \alpha_d) - \theta(\phi', \alpha_d))} \right) \\ &= \frac{is}{4\pi^2} \sum_{m'=1}^s \int_0^{2\pi} d\phi \int_0^{2\pi} d\phi' e^{\frac{im'(\phi-\phi')}{s}} \sum_{l=-\infty}^{\infty} e^{l(\phi-\phi')} \left[\left(\frac{\partial}{\partial \phi} \langle m' | u_n(\phi, \alpha_d) \rangle \right) + i \frac{\partial \theta(\phi, \alpha_d)}{\partial \phi} \langle m' | u_n(\phi, \alpha_d) \rangle \right] \langle u_n(\phi', \alpha_d) | m' \rangle e^{i(\theta(\phi, \alpha_d) - \theta(\phi', \alpha_d))}. \end{aligned} \quad (84)$$

Applying the Poisson summation formula, $\sum_{l=-\infty}^{\infty} e^{l(\phi-\phi')} = 2\pi \delta(\phi - \phi')$, we arrive at

$$\langle I_d \rangle = \frac{is}{2\pi} \int_0^{2\pi} d\phi \sum_{m'=1}^s \left(\frac{\partial}{\partial \phi} \langle m' | u_n(\phi, \alpha_d) \rangle \right) \langle u_n(\phi, \alpha_d) | m' \rangle - \frac{s}{2\pi} \int_0^{2\pi} d\phi \frac{\partial \theta(\phi, \alpha)}{\partial \phi} \sum_{m'=1}^s |\langle m' | u_n(\phi, \alpha_d) \rangle|^2. \quad (85)$$

The second term vanishes because $\sum_{m'=1}^s |\langle m' | u_n(\phi, \alpha_d) \rangle|^2 = 1$ and $\int_0^{2\pi} d\phi \frac{\partial \theta(\phi, \alpha_d)}{\partial \phi} = \theta(2\pi) - \theta(0) = 0$. The momentum expectation simplifies to a compact form:

$$\langle I_d \rangle = \frac{1}{2\pi} \int_0^{2\pi} d\phi \langle \bar{u}_n(\phi, \alpha_d) | is \frac{\partial}{\partial \phi} | \bar{u}_n(\phi, \alpha_d) \rangle. \quad (86)$$

Here, the identity $\langle \bar{u}_n(\phi, \alpha_d) | \frac{\partial}{\partial \phi} | \bar{u}_n(\phi, \alpha_d) \rangle = \sum_{m'=1}^s \left(\frac{\partial}{\partial \phi} \langle m' | u_n(\phi, \alpha_d) \rangle \right) \langle u_n(\phi, \alpha_d) | m' \rangle$ follows straightforwardly from the definition of $|\bar{u}_n(\phi, \alpha)\rangle$.

By considering the infinitesimal change in momentum over one adiabatic step, we can directly link the transport to the Berry curvature. To show this, we first examine the incremental change $\langle I_d \rangle - \langle I_{d-1} \rangle$. Using first-order perturbation theory, the Floquet eigenstate with parameter α_d can be expanded as

$$|\bar{u}_n(\phi, \alpha_d)\rangle = |\bar{u}_n(\phi, \alpha_{d-1})\rangle + |\bar{u}_n^{(1)}(\phi, \alpha_{d-1})\rangle, \quad (87)$$

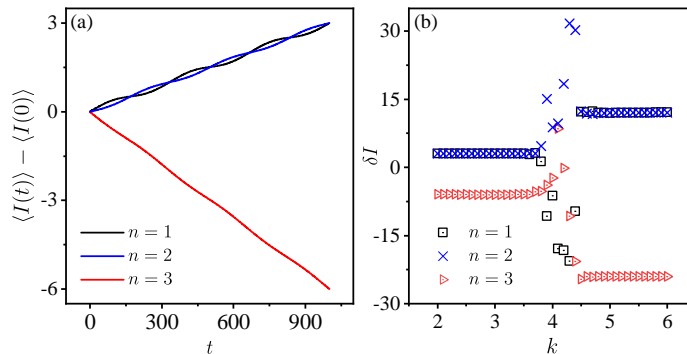


Fig. 12 (a) Time evolution of the average momentum during one adiabatic cycle for $k = 2.0$. (b) Change in the momentum expectation value after one adiabatic cycle implemented in $d_f = 1000$ discretized steps for different k . Here $T_0 = 2\pi/3$. (Adapted from [63].)

where

$$|\bar{u}_n^{(1)}(\phi, \alpha_{d-1})\rangle = \delta\alpha \sum_{n' \neq n} \frac{\langle \bar{u}_{n'}(\phi, \alpha_{d-1}) | \partial_{\alpha_{d-1}} \hat{U} | \bar{u}_n(\phi, \alpha_{d-1}) \rangle}{e^{i\omega_n} - e^{i\omega_{n'}}} |\bar{u}_{n'}(\phi, \alpha_{d-1})\rangle. \quad (88)$$

Using Eq. (86) and Eq. (87) and retaining terms linear in $\delta\alpha$, the momentum change can be expressed as

$$\begin{aligned} \langle I_d \rangle - \langle I_{d-1} \rangle &= \frac{is}{2\pi} \delta\alpha \int_0^{2\pi} d\phi \left[\langle \bar{u}_n^{(1)}(\phi, \alpha_{d-1}) | \frac{\partial}{\partial \phi} | \bar{u}_n(\phi, \alpha_{d-1}) \rangle + \langle \bar{u}_n(\phi, \alpha_{d-1}) | \frac{\partial}{\partial \phi} | \bar{u}_n^{(1)}(\phi, \alpha_{d-1}) \rangle \right] \\ &= \frac{is}{2\pi} \delta\alpha \int_0^{2\pi} d\phi \left[\langle \bar{u}_n^{(1)}(\phi, \alpha_{d-1}) | \frac{\partial}{\partial \phi} | \bar{u}_n(\phi, \alpha_{d-1}) \rangle - \left(\frac{\partial}{\partial \phi} \langle \bar{u}_n(\phi, \alpha_{d-1}) | \right) | \bar{u}_n^{(1)}(\phi, \alpha_{d-1}) \rangle \right]. \end{aligned} \quad (89)$$

Substituting the explicit form of $|\bar{u}_n^{(1)}(\phi, \alpha_{d-1})\rangle$ from Eq. (88) and using the relations in Eqs. (78) and (79), we finally obtain

$$\langle I_s \rangle - \langle I_{s-1} \rangle = -\frac{s}{2\pi} \int_0^{2\pi} d\phi B_n(\phi, \alpha_{d-1}) \delta\alpha, \quad (90)$$

where $B_n(\phi, \alpha)$ is exactly the Berry curvature we obtained in Eq. (80). Summing over a full adiabatic cycle, the total momentum expectation change is

$$\delta I = -s \int_0^{2\pi} d\phi \int_0^{2\pi} d\alpha B_n(\phi, \alpha) \delta\alpha = -s C_n, \quad (91)$$

where C_n is the Chern number of the n th Floquet band. This elegant relation shows that each complete cycle in α pumps an integer number of momentum quanta, proportional to the Chern number of the occupied Floquet band. Hence, the double kicked rotor realizes a topological Thouless pump in momentum space.

Detailed results are shown in Fig. 12, which almost perfectly match the analysis, except near the breakdown around some critical value of k . This deviation arises because, when a topological phase transition is about to occur, the associated band gaps become too small to guarantee adiabaticity, leading to imperfect quantization of the pumping process.

It is worth mentioning that the topological phenomena observed in above double kicked rotor are deeply rooted in its mathematical equivalence to the kicked Harper model [66], whose quasi-energy spectrum possesses a topologically non-trivial fractal structure characterized by non-zero Chern numbers associated with each spectral band.

Building upon the success of the standard double kicked rotor model in revealing non-equilibrium topological phases, a powerful generalization is the spin-1/2 double kicked rotor [64, 65]. To explore a broader landscape of topological phases, the model incorporates an internal spin-1/2 degree of freedom, allowing for both spin-dependent and spin-independent kicks, as described by the Floquet operator

$$\hat{U} = \exp\left(i\frac{\pi}{2}\hat{I}^2 \otimes \hat{\sigma}_0\right) \exp(-i\hat{H}_2) \exp\left(-i\frac{\pi}{2}\hat{I}^2 \otimes \hat{\sigma}_0\right) \exp(-i\hat{H}_1), \quad (92)$$

where each kick Hamiltonian \hat{H}_j ($j = 1, 2$) is given by

$$\hat{H}_j = K_j^0 \cos(v_j^0 \hat{\theta} + \alpha_j^0) \otimes \hat{\sigma}_0 + K_j \cos(v_j \hat{\theta} + \alpha_j) \otimes \hat{n}_j \cdot \hat{\sigma}. \quad (93)$$

Note that the system is on resonance condition, the Floquet operator is block diagonal in terms of the ‘‘Bloch wave number’’ ϕ . Therefore, it is convenient to describe the symmetry property in terms of the Floquet operator $\hat{U}(\phi)$. According to the Altland-Zirnbauer (AZ) classification, the time-reversal symmetry, the particle-hole symmetry, and the chiral symmetry for

the Floquet operator are respectively given by [67]:

$$\hat{T}\hat{U}(\phi)\hat{T}^{-1} = \hat{U}^{-1}(-\phi), \quad \hat{C}\hat{U}(\phi)\hat{C}^{-1} = \hat{U}(-\phi), \quad \hat{\Gamma}\hat{U}(\phi)\hat{\Gamma}^{-1} = \hat{U}^{-1}(\phi), \quad (94)$$

where \hat{T} , \hat{C} and $\hat{\Gamma}$ are time-reversal, particle-hole, and chiral operators, respectively. Based on these symmetries, one-dimensional topologically nontrivial topological phases can belong to several AZ classes [67]. Crucially, it has been shown that all kinds of one-dimensional topological phases can be achieved through the spin-1/2 double kicked rotor system by carefully designing the value of the parameters ν_j^0, α_j^0 and ν_j, α_j [65]. For example, the CII class (with $\hat{T}^2 = \hat{C}^2 = -1$) can be realized when all kicking frequencies $\nu_{1,2}^0, \nu_{1,2}$ are all odd integers, and the lattice phases are chosen to satisfy $\alpha_1^0 = 0, \alpha_1 = \pi/2, \alpha_2^0 = \pi/2$, and $\alpha_2 = 0$ [65].

The rich topological structure exhibited by the kicked rotor and its variants establishes it as a robust, non-equilibrium platform for a wide range of physical investigations. Recent advances have successfully extended these studies to incorporate effects such as non-Hermitian physics [68] and the observation of higher-order topological phases [69] in extended kicked rotor systems, highlighting their capability to model complex and frontier phenomena in condensed matter physics.

3.3 Scaling theory and Anderson transition

In Sec. 2.4, we established that dynamical localization in the kicked rotor can be mapped onto Anderson localization. The one-parameter scaling theory provides a powerful framework for analyzing localization phenomena and phase transitions in the standard Anderson model. According to this theory, disordered systems can be classified into three distinct regimes: the localized phase, where wave functions are exponentially confined and transport is strongly suppressed; the metallic phase, characterized by extended states and diffusive transport; and the critical phase at the metal-insulator transition, where the system displays scale-invariant behavior and multifractal eigenstates. In what follows, we briefly introduce the one-parameter scaling theory [41] and then discuss how it can be adapted to the kicked rotor model [70]. Finally, we summarize some recent advances in exploring the Anderson transition within this framework [71, 72, 73].

The core concept of one-parameter scaling theory is the dimensionless conductance g , whose scaling behavior is captured by the function $\beta(g)$, introduced by Edwards and Thouless [74]. This conductance is defined as the ratio of the Thouless energy E_c to the mean level spacing Δ , which typically scales as $\Delta \propto 1/L^d$, where L is the system's linear size and d its spatial dimensionality. The Thouless energy characterizes the energy scale associated with the time required for a particle to diffuse across the sample. In the semiclassical limit, it can be expressed as $E_c = \hbar D_{\text{cl}}/L^2$ where D_{cl} is the classical diffusion constant. Combining these expressions yields the scaling relation $g \propto L^{d-2}$ for diffusive systems. In contrast, when quantum interference leads to exponential localization of the wavefunction, the conductance behaves as $g \propto \exp(-L/\xi)$ where ξ is the localization length. Thus qualitatively, in the thermodynamic limit $L \rightarrow \infty$, the dimensionless conductance diverges ($g \rightarrow \infty$) in the metallic phase, while it vanishes ($g \rightarrow 0$) in the insulating phase. The dependence of g on the system size therefore serves as a diagnostic for localization. To formalize this, one defines the scaling function $\beta(g) = \partial \log(g(L))/\partial \log(L)$. From the above, we find $\beta(g) = d - 2$ for a classical metal (neglecting quantum corrections), and $\beta(g) = \log(g) < 0$ for an insulator. Assuming that $\beta(g)$ is a continuous and monotonic function, and that the variation of the conductance with system size depends only on the conductance itself, we can analyze how localization corrections depend on the spatial dimensionality d . When $d = 1$, for $g \rightarrow \infty$, $\beta(g) \rightarrow -1 < 0$ and for $g \rightarrow 0$, $\beta(g) = \log(g) < 0$. Therefore $\beta(g) < 0$ for any g , and the dimensionless conductance always decreases with the system size and the system will be an insulator in the $L \rightarrow \infty$ no matter the amount of disorder. When $d = 2$, for $g \rightarrow \infty$, $\beta(g) \rightarrow 0$ and for $g \rightarrow 0$, $\beta(g) = \log(g) < 0$. We have to determine whether $\beta(g)$ is positive or negative (or it remains zero) once quantum interference effects are included. When $d = 3$, for $g \rightarrow \infty$, $\beta(g) \rightarrow 1$ and for $g \rightarrow 0$, $\beta(g) = \log(g) < 0$. Since $\beta(g)$ is continuous and monotonous there must be $g = g_c$ such that $\beta(g_c) = 0$. At $g = g_c$ the system undergoes a metal-insulator transition. All these analysis are summarized in the schematic plot shown in fig. 13.

Now let us see how the one-parameter scaling theory can be adapted to the context of the kicked rotor. In this system, the mean level spacing Δ is well defined; the main challenge lies in defining the Thouless energy. In the Anderson model, the Thouless energy is typically estimated after averaging over many disorder realizations. Since localization in the kicked rotor is defined in momentum space, our task is to determine a typical and meaningful travel time associated with the exploration of the momentum basis. Intuitively, the ensemble average in the Anderson model can be replaced by an average over initial conditions in the kicked rotor. However, in mixed systems, the result depends sensitively on the choice of initial conditions: if the particle is initially located in an integrable region, the typical diffusion time will be larger than in a chaotic region, since KAM barriers slow down transport in momentum space. Therefore, to properly define the dimensionless conductance in the kicked rotor, we must impose the condition that the classical phase space is homogeneous. Under this assumption, a characteristic travel time can be defined unambiguously.

We are now ready to define g and construct the one-parameter scaling theory for the kicked rotor. Because the classical dynamics of this system is not always purely diffusive, we take into account a generalized diffusion behavior: $\langle \hat{I}^2 \rangle \sim t^\mu$ with $\mu > 0$. The Thouless energy is then given by $E_c \propto N^{-\frac{2}{\mu}}$, with N Hilbert space size. Also, for the mean level spacing we consider the general form $\Delta \propto N^{-\frac{2}{d_e}}$, which accommodates singular continuous spectrum (fractal or multifractal spectral), typically emerging at critical points. Here d_e is the effective spectral (fractal) dimension of the energy spectrum that characterizes how densely the spectrum fills the energy axis. For a normal spectrum one has $d_e = 1$, whereas at critical points the spectrum

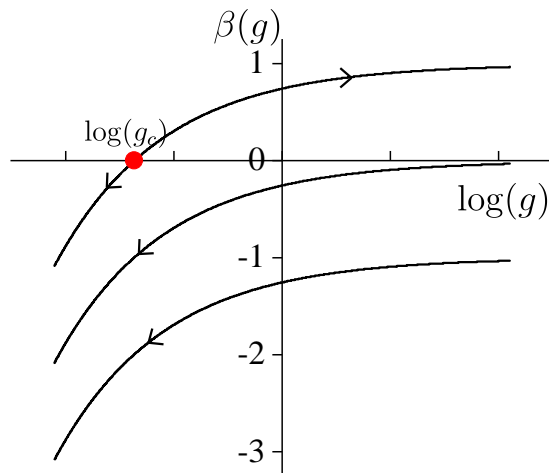


Fig. 13 Schematic plot of the dimensionless conductance β as a function of $\log(g)$ in different spatial dimensions ($d = 1, 2, 3$, shown from bottom to top).

becomes singular continuous, corresponding to $0 < d_e < 1$. The dimensionless conductance then becomes

$$g(N) = \frac{E_c}{\Delta} = N^{\gamma_{cl}}, \quad \gamma_{cl} = \frac{d}{d_e} - \frac{2}{\mu}. \quad (95)$$

In order to study how quantum effects modify the dimensionless conductance with increasing system size, we can define the scaling function

$$\beta(g) = \frac{\partial \log(g(N))}{\partial \log(N)}. \quad (96)$$

In cases where quantum effects are negligible, we have

$$\beta(g) = \gamma_{cl} = \frac{d}{d_e} - \frac{2}{\mu}. \quad (97)$$

Under the assumptions of the one-parameter scaling theory and using Eq. (97), we can propose the following definition of universality classes in kicked rotor systems: (i) If $\gamma_{cl} > 0$, the eigenfunctions are delocalized, as in a metallic phase, and the spectral correlations follow Wigner–Dyson statistics; (ii) If $\gamma_{cl} < 0$, the eigenfunctions are localized, as in an insulating phase, and the spectral correlations follow Poisson statistics; (iii) If $\gamma_{cl} = 0$, the eigenfunctions are multifractal, an insulator–metal transition occurs, and the spectral correlations are universally described by critical statistics. When the spectral dimension is normal, $d_e = 1$, the one parameter scaling theory predicts that if the classical motion is such that $\mu < \frac{2}{d}$ the quantum properties are those of an insulator, regardless of whether the classical motion is chaotic. For instance, in $d = 3$, any classical motion with $\mu < \frac{2}{3}$ drives the quantum system into the insulating phase—even if the classical dynamics is fully chaotic. Another illustrative example is the standard one-dimensional kicked rotor with a smooth potential. Although the classical dynamics typically exhibits normal diffusion $\mu = 1$, the resulting exponent $\gamma_{cl} = -1 < 0$ implies that the system resides in the insulating phase. Notably, Eq. (97) also suggests the possibility of a metal–insulator transition even in dimensions $d < 3$, potentially driven by superdiffusive classical motion [70, 75]. All these predictions highlight a remarkable feature of the scaling approach: dynamical phases can be inferred purely from classical transport properties and its spectral dimension, without requiring an explicit mapping to a lattice model.

To assess the robustness of the above semiclassical analysis, we examine the impact of quantum corrections. Quantum effects, such as destructive interference, are known to suppress or even halt transport, raising the question of whether the semiclassical predictions remain valid. For clarity, we focus on the case $d = 1$ and $d_e = 1$, where classical diffusion is governed by a fractional Fokker–Planck equation [76]:

$$\left(\frac{\partial}{\partial t} - D_{cl} \frac{\partial^{2/\mu}}{\partial |p|^{2/\mu}} \right) P(p, t) = \delta(p) \delta(t). \quad (98)$$

Applying a Fourier transform from (p, t) space to (q, ω) space yields the classical propagator:

$$K_0(q, \omega) = \frac{\nu}{-i\omega + D_{cl}|q|^{2/\mu}}, \quad (99)$$

where ν is a constant prefactor related to the density of states. The one-loop corrected propagator $K(q, \omega)$ modify this

classical propagator $K_0(q, \omega)$ via the Dyson equation:

$$K^{-1}(q, \omega) = K_0^{-1}(q, \omega) - \Sigma(q, \omega), \quad (100)$$

where the self-energy correction Σ accounts for interference corrections originating from intermediate momentum modes k :

$$\Sigma(q, \omega = 0) = C_0 \int \frac{|q + k|^\alpha - |k|^\alpha}{|k|^\alpha} dk. \quad (101)$$

To evaluate this integral, we use the expansion [77]:

$$\frac{|q + k|^{2/\mu}}{|k|^{2/\mu}} - 1 \simeq \begin{cases} \frac{2}{\mu} \frac{qk}{k^2} + \frac{1}{\mu} \frac{q^2}{k^2} + \frac{2}{\mu} \left(\frac{1}{\mu} - 1\right) \left(\frac{qk}{k^2}\right)^2 + \dots, & q \ll k, \\ \frac{|q|^{2/\mu}}{|k|^{2/\mu}}, & q \gg k, \end{cases} \quad (102)$$

The quantum diffusion coefficient D_{qu} to this order is easily obtained as

$$D_{\text{qu}} = D_{\text{cl}} - \frac{\nu \Sigma(q, \omega = 0)}{|q|^{2/\mu}} = \begin{cases} D_{\text{cl}} - CN^{2/\mu-1}, & 1 < 2/\mu < 2, \\ D_{\text{cl}} - C \ln(qN), & 2/\mu = 1, \\ D_{\text{cl}} - Cq^{1-2/\mu}, & 0 < 2/\mu < 1, \end{cases} \quad (103)$$

where C is a different constant for each case. The quantum correction to the diffusion constant depends critically on the exponent $2/\mu$, which characterizes the scaling behavior of the classical propagator in momentum space. This parameter governs the infrared divergence of the one-loop interference integral: when $2/\mu > 1$, the correction grows with system size, indicating strong quantum interference and potential localization. For $2/\mu < 1$, the correction is subleading and the classical diffusion remains stable. The marginal case $2/\mu = 1$ corresponds to a metal-insulator transition, where the correction becomes logarithmic, reminiscent of two-dimensional disordered systems. Thus, $2/\mu$ serves as a key indicator of whether quantum interference destabilizes classical transport.

The one-parameter scaling theory has been tested across various versions of the kicked rotor model. Of particular interest is the kicked rotor with a singular potential [75], described by the Hamiltonian

$$H = \frac{\hat{I}^2}{2} + V(\hat{\theta}) \sum \delta(t - n), \quad (104)$$

where the kicking potential $V(\hat{\theta})$ takes the form

$$V(\hat{\theta}) = K|\hat{\theta}|^\alpha, \alpha \in [-1, 1], \quad \text{or} \quad V(\hat{\theta}) = K \log(|\hat{\theta}|). \quad (105)$$

Note that the logarithmic singularity corresponds to the limiting case $\alpha = 0$ because $\lim_{\alpha \rightarrow 0} \frac{|\theta|^\alpha - 1}{\alpha} = \log|\theta|$. The classical dynamics of this system exhibits markedly different behavior depending on the singularity exponent α . For $\alpha > 1/2$ the second moment of the momentum increments is finite, $\langle I^2 \rangle < \infty$, leading to normal diffusion $\langle I^2 \rangle \sim Dt$, and the corresponding quantum dynamics display Poissonian spectral statistics, consistent with the prediction of the one-parameter scaling theory for localized regimes. In contrast, for $\alpha < 1/2$ the variance diverges, $\langle \Delta I^2 \rangle = \infty$, the central limit theorem fails, and the dynamics exhibits superdiffusive (Lévy-type) momentum spreading. According to Eq. (97), the dimensionless conductance scales as

$$\beta_{\text{cl}}(g) = -\frac{\alpha}{1 - \alpha}. \quad (106)$$

For $\alpha > 0$, the scaling theory predicts an insulating phase regardless of quantum corrections. For $\alpha < 0$, it predicts a metallic phase, as quantum interference does not qualitatively alter the classical transport. The marginal case $\alpha = 0$ (logarithmic singularity) marks a critical phase. Taken together, these results demonstrate that dynamical localization can be overcome, even in one dimension.

While the one-parameter scaling theory captures how localization and spectral properties depend on the momentum-space size N , it is intrinsically a static framework and cannot describe the detailed time evolution of wave packets. In contrast, recent works extended the scaling approach to explicitly include dynamics [71]. They demonstrated that for the logarithmic kicked rotor, where the system resides at the critical point predicted by one-parameter scaling, the quantum dynamics follow a genuine two-parameter scaling law involving both N and the evolution time t . This formulation successfully characterizes the temporal spreading and multifractal correlations of critical wave packets, providing a dynamical generalization of the conventional one-parameter scaling framework. This was further generalized to effectively infinite-dimensional Anderson transitions [72, 73], revealing a novel logarithmic multifractal phase. In this regime, critical observables scale with $\ln(N)$ and $\ln(t)$ rather than conventional power laws, marking a distinct universality class of criticality in disordered quantum systems. In short, these advances establish the kicked rotor as a paradigmatic and experimentally accessible platform for exploring Anderson transitions, critical phases and the dynamical facets of quantum criticality.

3.4 Spin-1/2 kicked rotor

In previous subsections, we have shown that on-resonance spin-1/2 kicked rotor can be harnessed to engineer a wide variety of topological phases. Surprisingly, even away from resonance, where the classical system becomes fully chaotic and no Bloch-type quantum numbers exist, topological physics re-emerges in a completely different form. In the nonresonant, chaotic regime, a phenomenon known as Planck's quantum-driven integer quantum hall effect [78, 79] closely mimics the integer quantum Hall effect (IQHE) despite the absence of any magnetic field or Fermi statistics. In the following, we first present the conceptual framework that illustrates how topology can emerge from chaos, and then discuss some recent advances.

The quantum dynamics of the model under consideration are governed by

$$i\hbar_{\text{eff}} \partial_t \tilde{\psi}_t = \hat{H}(t) \tilde{\psi}_t, \quad \hat{H}(t) = \frac{1}{2} \hat{I}_1^2 + \sum_{\alpha} V_{\alpha}(\hat{\theta}_1, \hat{\theta}_2 + \tilde{\omega}t) \sigma_{\alpha} \sum_{n \in \mathbb{Z}} \delta(t - n), \quad (107)$$

where the quantity $\tilde{\omega}/2\pi$ is assumed to be irrational. The spin-dependent kicking potentials V_{α} exhibit specific parity properties: V_x is odd in θ_1 and even in θ_2 ; V_y is even in θ_1 and odd in θ_2 ; and V_z is even in both θ_1 and θ_2 . In the following we focus on the rotor's dimensionless kinetic energy

$$E(t) \equiv -\frac{1}{2} \langle \langle \psi_t | \partial_{\theta_1}^2 | \psi_t \rangle \rangle_{\theta_2}, \quad (108)$$

where $\langle \rangle_{\theta_2}$ denotes the average over the prescribed phase θ_2 . For simplicity, we assume that the initial state is uniform in θ_1 . The long-time behavior of $E(t)$ characterizes the rotor's transport properties: a vanishing asymptotic growth rate, $\lim_{t \rightarrow \infty} \frac{E(t)}{t} = 0$, corresponds to bounded motion in angular momentum space, analogous to insulating behavior in disordered electronic systems. Conversely, a nonzero growth rate indicates unbounded motion, mimicking metallic transport. In the following we will see that only for a discrete set of critical values of \hbar_{eff} can $E(t)$ increase linearly at large t , which bears a close resemblance to the integer quantum Hall effect.

To see how topological structure can emerge from this one-dimensional model, we first reinterpret the system as a two-dimensional periodic one by treating the parameter θ_2 as a "virtual" dynamical variable. This construction effectively maps the original one-dimensional system into a higher-dimensional parameter space, allowing us to explore topological features that are otherwise inaccessible in strictly one-dimensional settings. This is achieved by performing the following gauge-like transformation:

$$\hat{H} \longrightarrow e^{\tilde{\omega}t \partial_{\theta_2}} \hat{H} e^{-\tilde{\omega}t \partial_{\theta_2}}, \quad \tilde{\psi}_t \longrightarrow e^{-\tilde{\omega}t \partial_{\theta_2}} \tilde{\psi}_t \equiv \psi_t. \quad (109)$$

Substituting Eq. (109) into Eq. (107), the transformed Schrödinger equation becomes

$$i\hbar_{\text{eff}} \partial_t \psi_t = \left(\frac{1}{2} \hat{I}_1^2 + \tilde{\omega} \hat{I}_2 + \sum_{\alpha} V_{\alpha}(\hat{\theta}_1, \hat{\theta}_2) \sigma_{\alpha} \sum_{n \in \mathbb{Z}} \delta(t - n) \right) \psi_t, \quad (110)$$

where $\hat{I}_2 = -i\hbar_{\text{eff}} \partial_{\theta_2}$ is the conjugate variable of θ_2 . The Floquet operator for the two-dimensional system reads

$$\hat{U} = \exp\left(-\frac{i}{\hbar_{\text{eff}}} \left(\frac{1}{2} \hat{I}_1^2 + \tilde{\omega} \hat{I}_2 \right)\right) \exp\left(-\frac{i}{\hbar_{\text{eff}}} \sum_{\alpha} V_{\alpha}(\theta_1, \theta_2) \sigma_{\alpha}\right). \quad (111)$$

Here, the terms $V_x \sigma_x + V_y \sigma_y$ mimics a 2D "spin-orbit coupled" electron, with $\Theta \equiv (\theta_1, \theta_2)$ playing the role of its "momentum". Meanwhile, $V_z \sigma_z$ acts as a "Zeeman coupling", explicitly breaking the effective time-reversal symmetry $i\sigma_y \mathcal{K}$ (\mathcal{K} is the combination of complex conjugation and the operation: $\theta_{1,2} \rightarrow -\theta_{1,2}$, $\hat{I}_{1,2} \rightarrow \hat{I}_{1,2}$). The first exponential in Eq. (111) induces oscillations in angular momenta, which can be interpreted as disorder localized at the "position" $N \equiv (n_1, n_2)$ due to incommensurability, where n_1 and n_2 are the eigenvalues of \hat{I}_1 and \hat{I}_2 . Thus, this analogy already hints at an IQHE-like topological behavior driven purely by quantum interference.

Starting from the two-dimensional dynamics, the rotor's kinetic energy, Eq. (108), can be rewritten as

$$E(t) = \frac{1}{2} \sum_{N, N'} \sum_{s_{\pm}, s'_{\pm}} \langle \psi_0 | \hat{U}^{-t} | N, s_- \rangle \langle N, s_- | \hat{n}_1^2 | N, s_+ \rangle \langle N, s_+ | \hat{U}^t | N', s'_+ \rangle \langle N', s'_+ | \psi_0 \rangle \langle \psi_0 | N', s'_- \rangle. \quad (112)$$

Using the resolvent representation of the Floquet operator,

$$\hat{U}^t = \int_0^{2\pi} \frac{d\omega_+}{2\pi} e^{+i\omega_+ t} \frac{1}{1 - e^{+i\omega_+} \hat{U}}, \quad \hat{U}^{-t} = \int_0^{2\pi} \frac{d\omega_-}{2\pi} e^{-i\omega_- t} \frac{1}{1 - e^{-i\omega_-} \hat{U}^\dagger}, \quad (113)$$

and defining $\omega_{\pm} = \omega_0 \pm \omega/2$, one obtains

$$E(t) = \frac{1}{2} \int_0^{2\pi} \frac{d\omega}{2\pi} e^{-i\omega t} \sum_{N, N'} \sum_{s_{\pm}, s'_{\pm}} \delta_{N', 0} \delta_{s_+, s_-} n_1^2 K_{\omega}(N s_+, s_-, N' s'_+, s'_-) \psi_{0, s'_+} \psi_{0, s'_-}^*. \quad (114)$$

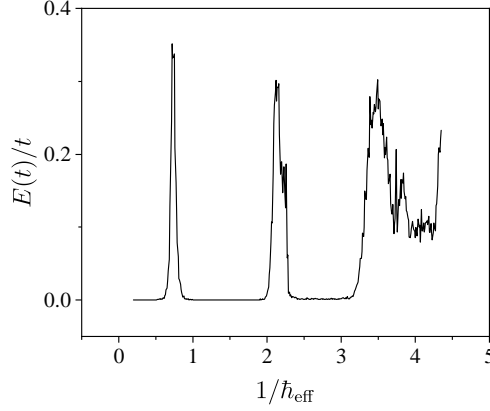


Fig. 14 Energy growth rate of the spin-1/2 kicked rotor for different values of \hbar_{eff} . The kicking potentials are set as $V_x = \frac{2 \arctan(2|\mathbf{d}|)}{|\mathbf{d}|} d_1$, $V_y = \frac{2 \arctan(2|\mathbf{d}|)}{|\mathbf{d}|} d_2$, and $V_z = \frac{2 \arctan(2|\mathbf{d}|)}{|\mathbf{d}|} d_3$, with $\mathbf{d} = (d_1, d_2, d_3) = (\sin \theta_1, \sin \theta_2, 0.8(1 - \cos \theta_1 - \cos \theta_2))$. (Adapted from [79].)

Here the two-particle correlation function is defined as

$$K_\omega(Ns_+s_-, N's'_+s'_-) = \left\langle \langle Ns_+ | \frac{1}{1 - e^{+i\omega_+} \hat{U}} | N's'_+ \rangle \langle N's'_- | \frac{1}{1 - e^{-i\omega_-} \hat{U}^\dagger} | Ns_- \rangle \right\rangle_{\omega_0}. \quad (115)$$

Physically, K_ω encodes the interference between advanced and retarded quantum amplitudes propagating on the angular-momentum lattice $N = (n_1, n_2)$. To evaluate such a correlation function, it can be cast into a functional-integral form over a supermatrix field $Z \equiv \{Z_{Ns, N's'\alpha'}\}$ schematically as

$$K_\omega \sim \int D(Z, \tilde{Z}) e^{-S[Z, \tilde{Z}]}, \quad (116)$$

where $S[Z, \tilde{Z}]$ is an effective action reflecting the interference between advanced (+) and retarded (-) sectors. It is convenient to introduce the Wigner representation

$$Z_{N,\Theta} = \sum_{\Delta N} e^{-i\Delta N \Theta} Z_{N_1, N_2}, \quad (117)$$

with $\Delta N = N_1 - N_2$ and $N = (N_1 + N_2)/2$. In this picture, the variable Θ acts as a velocity-like coordinate, while the off-diagonal components in angular momentum ($\Delta N \neq 0$) correspond to velocity fluctuations.

When the system exhibits strong chaos, correlations between distinct lattice points $N \neq N'$ decay rapidly. In this case, the off-diagonal components $Z_{N \neq N'}$ represent short-lived fluctuations and can be averaged out, leaving a smooth, slowly varying field $Z(N) \equiv Z_{N,N}$, defined on the two-dimensional lattice. The field $Z(N)$ now depends only on the coarse-grained coordinates and describes the long-time interference between advanced and retarded components.

Because of its internal structure, $Z(N)$ defines a mapping from the effective phase space (N, Θ) to a geometric target space associated with the unitary symmetry of the system. The target manifold is topologically equivalent to the direct product of a hyperbolic plane H^2 and a two-sphere S^2 , i.e. $(H^2 \times S^2)_{\text{target}}$. Physically, the H^2 sector represents diffusive spreading of amplitudes in angular-momentum space, while the compact S^2 part captures the relative phase (or spin-like) structure that carries topological information.

In the chaotic regime, the dynamics explores the entire two-dimensional lattice ergodically, so the mapping can wrap the compact S^2 component an integer number of times. All such mappings are classified by

$$\pi_2(H^2 \times S^2) = \pi_2(H^2) \times \pi_2(S^2) = \pi_2(S^2) = \mathbb{Z}. \quad (118)$$

Because H^2 is noncompact, it has no topological contribution, leaving only the integer-valued winding of the S^2 component as the relevant topological invariant. This integer characterizes the quantized transport emerging from the underlying chaotic dynamics of the rotor. Further details of the effective field theory for the spin-1/2 quantum kicked rotor case can be found in [79].

For rational $\tilde{\omega}/(2\pi)$, the system acquires translational invariance along the \hat{I}_2 direction. Due to this symmetry, the propagation along \hat{I}_2 becomes ballistic at long times, while motion along \hat{I}_1 loses memory of its initial velocity. The effective two-dimensional diffusion is thus replaced by quasi-one-dimensional dynamics, and the mapping $Z(N) \rightarrow (H^2 \times S^2)$ becomes topologically trivial:

$$\pi_1(H^2 \times S^2) = \pi_1(H^2) \times \pi_1(S^2) = 0. \quad (119)$$

Table 1 The analogy between Planck's quantum-driven integer Quantum Hall effect and conventional integer Quantum Hall effect. (Adapted from [79].)

	Planck's quantum-driven	Conventional
System	Spin- $\frac{1}{2}$ quasiperiodic quantum kicked rotor	2D electron gas
Driving parameter	Planck's quantum \hbar_{eff}	Magnetic field
Characteristic of dissipation	Energy growth rate $\lim_{t \rightarrow \infty} \frac{E(t)}{t}$	Longitudinal conductivity
Characteristic of topology	Hidden quantum number σ_{H}^*	Quantized Hall conductivity
Characteristic of insulator	$\lim_{t \rightarrow \infty} \frac{E(t)}{t} = 0$	Vanishing longitudinal conductivity
Characteristic of metal	$\lim_{t \rightarrow \infty} \frac{E(t)}{t} = \sigma^*$	Finite longitudinal conductivity

Hence, the topological invariant vanishes and no quantized insulating phase appears in the rational case.

The above analysis relies crucially on the assumption of strong chaos, which ensures rapid decay of correlations and justifies the reduction to a smooth field $Z(N)$. Interestingly, recent studies have revealed that phenomena resembling the integer quantum Hall effect can also emerge in nonchaotic systems [80]. Specifically, the spin-Maryland model, an integrable, self-dual extension of the standard Maryland rotor [81], exhibits quantized transitions between dynamically localized and delocalized phases [80]. There, the quantization originates not from ergodic mixing, but from an exact spectral self-duality that maps the angular and momentum representations onto each other, leading to a topological classification of dynamical phases, where each phase is indexed by a topological invariant in the parameter (effective Planck constant) space. These findings demonstrate that topological quantization can emerge through distinct physical routes: either from chaotic mixing in the spin-1/2 kicked rotor, or from exact self-duality in the integrable spin-Maryland model. Together, they highlight the remarkable richness of dynamical behavior in spinful kicked-rotor systems, where chaos, integrability, and topology are deeply intertwined.

3.5 Coupled kicked rotors

In the above discussion, our attention has primarily been restricted to the (effective) single-body kicked rotor model, which already exhibits a variety of nontrivial dynamical behaviors. Recent studies, however, have extended this framework to the many-body domain, giving rise to the coupled kicked rotor system. Even when only two rotors are coupled, the dynamical landscape becomes considerably richer: the interplay between periodic driving and inter-rotor interaction generates complex entanglement dynamics, which plays a central role in diagnosing thermalization and localization in interacting quantum systems [82]. In what follows, we first introduce the transport and entanglement dynamics in the coupled kicked rotor through a representative example [83], and then briefly outline some of the recent frontiers in coupled kicked rotor model.

The Floquet operator for the two-body coupled kicked rotor we consider here is given by

$$\hat{U} = \exp\left(-i\left(\frac{\hat{I}_1^2}{2} + \frac{\hat{I}_2^2}{2}\right)\right) \exp\left(-i\left(K_1 \cos \hat{\theta}_1 + K_2 \cos \hat{\theta}_2 + \xi \cos(\hat{\theta}_1 - \hat{\theta}_2)\right)\right), \quad (120)$$

Hereafter we focus on the parameter regime in which the single-body kicking strengths K_j are sufficiently large, while the inter-rotor coupling strength ξ is small. We consider as initial state product states of the form

$$|\Psi(0)\rangle = |\psi_1(0)\rangle \otimes |\psi_2(0)\rangle, \quad (121)$$

where $|\psi_j(0)\rangle$ is a coherent state of j th rotor.

We begin by examining the energy-transport properties of the j th rotor, defined by $E_j(t) = \langle \Psi(t) | \frac{\hat{I}_j^2}{2} | \Psi(t) \rangle$. When $\xi = 0$, each rotor exhibits dynamical localization independently at around its diffusion timescale t_b . As discussed previously, the destructive quantum interference between multiple scattering paths in angular momentum space leads each rotor to dynamical localization, thereby suppressing energy diffusion. However, the coupled system (120) modifies this picture in a subtle way. The interaction

$$H_I = \xi \cos(\hat{\theta}_1 - \hat{\theta}_2) \sum_{n \in \mathbb{Z}} \delta(t - n) \quad (122)$$

ouples the two rotors in angular position space at each kick. From a semiclassical viewpoint, one can regard rotor 2 as a time-dependent “force” acting on rotor 1 through the phase factor $e^{-i\xi \cos(\theta_1 - \theta_2)}$, and vice versa. For fully chaotic single-rotor dynamics, the relative phase $\theta_1 - \theta_2$ explores the interval $[0, 2\pi)$ in an effectively random manner. Consequently, the motion of one rotor induces stochastic phase modulation in the Floquet evolution of the other. This effective phase noise continuously perturbs the coherent interference pattern in angular momentum space that underlies dynamical localization, thereby destabilizing it.

This destabilization mechanism can be further clarified through the lattice-model mapping perspective. A single quantum kicked rotor maps onto a one-dimensional tight-binding Anderson model with static disorder in the on-site terms, where

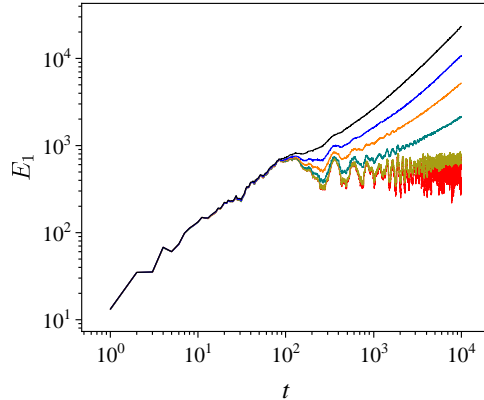


Fig. 15 Average energy of the first rotor, with $K_1 = 9.0$ and $K_2 = 10.0$. The coupling strengths are, from bottom to top, $\xi = 0, 0.01, 0.03, 0.05, 0.07$, and 0.1 (Adapted from [83]).

dynamical localization corresponds to Anderson localization in angular momentum space. In contrast, the coupled kicked rotors yield a Floquet matrix that maps onto an effective two-dimensional lattice model [84]. Importantly, the present coupling term $\xi \cos(\hat{\theta}_1 - \hat{\theta}_2)$ predominantly generates off-diagonal couplings between different momentum states, rather than simply renormalizing the on-site disorder. Such dynamically generated off-diagonal disorder invalidates the straightforward one-dimensional Anderson localization picture and is known to promote delocalization or anomalous diffusion in higher-dimensional effective lattices [85]. As a result, dynamical localization is no longer guaranteed to remain stable for arbitrarily long times once $\xi > 0$.

The above scenario naturally introduces two distinct and physically different time scales. The first one is the single-rotor quantum break time t_b , which is the time scale on which coherent backscattering in momentum space builds up and the classical diffusion is suppressed for an isolated kicked rotor. The second time scale, denoted by $t^*(\xi)$, is a genuine coupling-induced crossover time. It characterizes the onset of the destruction of dynamical localization due to the cumulative phase noise generated by the mutual interaction. Unlike t_b , the crossover time t^* diverges in the limit $\xi \rightarrow 0$ and therefore quantifies the stability of localization against inter-rotor coupling. For weak coupling one has the hierarchy $t_b \ll t^*(\xi)$.

Therefore, these considerations lead to a generic three-stage scenario for the energy growth of each rotor under weak but finite coupling: (1) For short times $t \lesssim t_b$, the quantum dynamics closely follows the classical chaotic diffusion, $E_j(t) \simeq D_{cl}t$, where D_{cl} denotes the classical diffusion coefficient. (2) At intermediate times $t_b \lesssim t \lesssim t^*(\xi)$, a regime of dynamical localization appears. Quantum interference still partially suppresses transport, so that $E_j(t)$ remains approximately constant over a broad temporal time window. (3) At long times $t \gtrsim t^*(\xi)$, the cumulative effect of the coupling-induced stochastic phase modulation destroys the residual quantum coherence. Dynamical localization is completely washed out and a genuine diffusive growth is restored, $E_j(t) \simeq D_q t$, with D_q the asymptotic quantum diffusion coefficient, generally different from D_{cl} . This three-stage scenario is fully corroborated by the numerical results shown in Fig 15.

We now turn to the entanglement dynamics. When $\xi = 0$, the system consists of two uncoupled kicked rotors and therefore no entanglement is generated during the time evolution. Introducing a nonzero coupling ξ induces correlations between the two subsystems, leading to the development of entanglement. For pure global states of a bipartite system, the standard measure of entanglement is the von Neumann entropy of the reduced density matrix of either subsystem, often referred to as the entanglement entropy [86], defined as

$$S_{vN}(t) = -\text{Tr}[\hat{\rho}_1(t) \log \hat{\rho}_1(t)], \quad (123)$$

where $\hat{\rho}_1(t) = \text{Tr}_2 |\Psi(t)\rangle\langle\Psi(t)|$ denotes the reduced density matrix of rotor 1 obtained by tracing out the degrees of freedom of rotor 2. The von Neumann entropy provides a complete characterization of bipartite entanglement, capturing both its growth and eventual saturation. For analytic purposes, however, it is often convenient to employ the linear entropy,

$$S_{lin}(t) = 1 - \text{Tr}[\hat{\rho}_1^2(t)]. \quad (124)$$

Although S_{lin} may not share the same scaling form as the von Neumann entropy, it can faithfully capture the dynamical crossover between different entanglement-growth regimes and allows for perturbative treatments in the weak-coupling regime.

Since the generation of entanglement is solely due to the inter-rotor coupling, it is convenient to analyze the dynamics in the interaction picture with respect to the uncoupled Hamiltonian. The interaction-picture transformation is defined as

$$\hat{\rho}^I(t) = \left(\exp\left(-i\left(\frac{\hat{I}_1^2}{2} + \frac{\hat{I}_2^2}{2}\right)\right) \exp\left(-i(K_1 \cos \hat{\theta}_1 + K_2 \cos \hat{\theta}_2)\right) \right)^{\dagger} \hat{\rho}(t) \left(\exp\left(-i\left(\frac{\hat{I}_1^2}{2} + \frac{\hat{I}_2^2}{2}\right)\right) \exp\left(-i(K_1 \cos \hat{\theta}_1 + K_2 \cos \hat{\theta}_2)\right) \right), \quad (125)$$

and the total density matrix obeys

$$\frac{d\hat{\rho}^l(t)}{dt} = -i[\hat{H}_l(t), \hat{\rho}^l(t)]. \quad (126)$$

As the initial state is a product state, we have $\hat{\rho}^l(0) = |\psi_1(0)\rangle\langle\psi_1(0)| \otimes |\psi_2(0)\rangle\langle\psi_2(0)|$. Performing formal integration and iteration and expanding to second order in ξ gives the result

$$\hat{\rho}^l(t) = \hat{\rho}^l(0) - i\xi \sum_{r=1}^t [\hat{F}(r), \hat{\rho}^l(0)] + (i\xi)^2 \sum_{r=1}^t \sum_{s=1}^{r-1} [\hat{F}(s), [\hat{F}(r), \hat{\rho}^l(0)]], \quad (127)$$

where $\hat{F}(r) = \cos(\hat{\theta}_1(r) - \hat{\theta}_2(r))$. Tracing over the second rotor and using the definition of linear entropy, one obtains

$$S_{\text{lin}}(t) = \xi^2 \sum_{r,s=1}^t C(r, s), \quad (128)$$

where $C(r, s)$ is a two-time correlation function of the interaction operator, defined as

$$C(r, s) = \text{Tr}_1 \left[\text{Tr}_2 \left([\hat{F}(r), \hat{\rho}^l(0)] \right) \text{Tr}_2 \left([\hat{F}(s), \hat{\rho}^l(0)] \right) \right]. \quad (129)$$

For fully chaotic single-rotor dynamics these correlations decay rapidly with $|r - s|$, and one finds numerically that $C(t) \propto t$. Consequently, the early-time entanglement growth is linear ¹¹,

$$S_{\text{lin}}(t) \propto \xi^2 t, \quad (130)$$

with a slope determined by the interaction strength ξ . This linear growth in the short-time regime is confirmed by the numerical results shown in fig. 16 (a).

The above perturbative expression is derived under the assumption that the total state remains close to a product state, i.e. that the correction $\delta\hat{\rho}^l(t)$ remains small compared to the unperturbed reduced density matrix $\hat{\rho}_1^{(0)}(t)$. This assumption breaks down once strong entanglement is formed at long times. In the diffusive regime of energy transport discussed above, the reduced phase-space distribution of each rotor becomes approximately Gaussian in angular momentum and nearly uniform in the angle coordinate. In this regime the reduced state is well described by a smooth Husimi function $\mathcal{H}(\theta_1, I_1)$, and the linear entropy can be expressed as [88]

$$S_{\text{lin}} = 1 - \int \frac{d\theta_1 dI_1}{2\pi} \mathcal{H}^2(\theta_1, I_1). \quad (131)$$

Approximating the Husimi function in the diffusive regime by a Gaussian in angular momentum, $\mathcal{H}(\theta_1, I_1) \simeq \sqrt{\frac{I_1}{2\pi D_q t}} \exp\left(-\frac{I_1^2}{2D_q t}\right)$, where D_q denotes the asymptotic quantum diffusion coefficient, one obtains the long-time asymptotic behavior as

$$S_{\text{lin}}(t) = 1 - \left(\frac{1}{4\pi D_q t} \right)^{1/2}. \quad (132)$$

Thus, in contrast to the early-time linear growth, the linear entropy approaches its maximal value only algebraically at long times, reflecting the diffusive broadening of the reduced phase-space distribution. It should be noted that the von Neumann entropy S_{vN} behaves differently from S_{lin} in this regime, since S_{lin} is bounded by unity by definition, whereas S_{vN} is unbounded. In the diffusive regime, the effective number of participating Schmidt modes—i.e., the number of nonzero coefficients in the Schmidt decomposition [44] of a pure bipartite quantum state into a sum of separable states—can be estimated from the Husimi distribution as $N_{\text{eff}}(t) \simeq \left(\int \frac{d\theta_1 dI_1}{2\pi} \mathcal{H}^2(\theta_1, I_1) \right)^{-1} \sim \sqrt{D_q t}$. Since the von Neumann entropy scales as $S_{\text{vN}} \sim \ln N_{\text{eff}}$, one obtains the long-time asymptotic behavior

$$S_{\text{vN}}(t) \simeq \frac{1}{2} \ln t + \text{const}, \quad (133)$$

which is also confirmed in Fig.16 (b).

In the above, we have focused on a specific model of coupled kicked rotors. More generally, coupled rotor systems provide a flexible and unifying framework for exploring interaction effects in periodically driven quantum systems. In particular, many-body coupled kicked rotors open the door to addressing a range of outstanding questions at the intersection of chaos, transport, and nonequilibrium dynamics. Within this class of models, interaction effects may lead to rich dynamical phenomena, including interaction-induced delocalization [89, 90, 91], subdiffusive transport [92], and the emergence of Arnold diffusion in high-dimensional phase space [93]. Overall, coupled kicked rotors offer a minimal and powerful setting to uncover universal features of interaction-driven dynamics in quantum systems.

¹¹It should be noted that Ref. [87] proved that, on short timescales, the entanglement entropy cannot exhibit linear growth. In the present model, however, the characteristic time scale is extremely short, and the time window considered here lies beyond this transient regime.

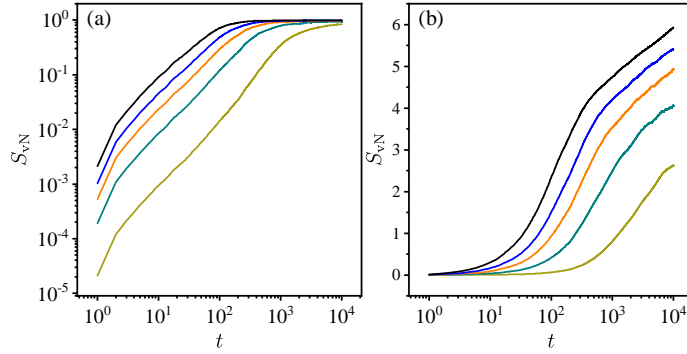


Fig. 16 Time evolution of the entanglement entropy. Panel (a) shows the results on a log-log scale, while panel (b) uses a log-linear scale. Parameters are $K_1 = 9.0$ and $K_2 = 10.0$. The coupling strengths are, from bottom to top, $\xi = 0.01, 0.03, 0.05, 0.07,$ and 0.1 . (Adapted from [83].)

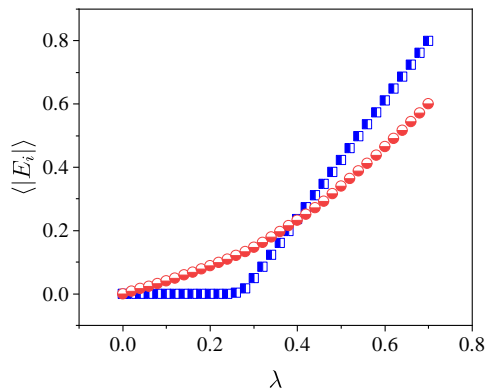


Fig. 17 Average imaginary part of the quasi-energy spectrum for $k = 3$. Blue squares correspond to $T = 1.4$ (localized regime), while red circles correspond to $T = \pi/3$ (resonant regime).

3.6 Non-Hermitian kicked rotor

In recent years, the rapid progress of non-Hermitian physics has offered new perspectives for exploring exotic quantum dynamics beyond the Hermitian paradigm. Within this framework, non-Hermitian extensions of the kicked rotor provide a minimal setting to investigate how quantum-interference phenomena, such as dynamical localization and quantum resonances, are modified by gain–loss mechanisms. We use a \mathcal{PT} -symmetric kicked rotor as an example to briefly introduce the interplay between the kicked rotor and non-Hermitian physics [94], followed by a short outlook.

A representative example of the Non-Hermitian kicked rotor is the \mathcal{PT} -symmetric kicked rotor described by the Floquet operator

$$\hat{U} = \exp\left(-i\frac{\hat{P}^2}{2}T\right)\exp\left[-iK(\cos\theta + i\gamma\sin\theta)\right], \quad (134)$$

where K denotes the Hermitian kicking strength and γ controls the amplitude of balanced gain and loss. The imaginary part of the kicking potential is odd in θ , ensuring \mathcal{PT} symmetry of the Floquet operator.

An central observation for this model is that, when $|\gamma| < 1$, the complex kicking potential can be rewritten as a complex-shifted function. By introducing

$$K_0 = K\sqrt{1-\gamma^2}, \quad \tanh\eta = \gamma, \quad (135)$$

the kicking potential can be transformed to

$$K(\cos\theta + i\gamma\sin\theta) = K_0\cos(\theta - i\eta), \quad (136)$$

i.e., the non-Hermitian kick is equivalent to an imaginary shift $\theta \mapsto \theta - i\eta$, accompanied by a renormalization of the kicking

strength, $K \rightarrow K_0$. This immediately suggests a mapping to a Hermitian kicked rotor. Let

$$\hat{U}_0 = \exp\left(-i\frac{f^2}{2} T\right) \exp(-iK_0 \cos \hat{\theta}) \quad (137)$$

be the unitary Floquet operator of the Hermitian kicked rotor with effective kick K_0 . The imaginary shift can be implemented by a non-unitary similarity transformation generated by \hat{I} . Defining

$$\hat{S} \equiv \exp(\eta \hat{I}), \quad (138)$$

one has $\hat{S}^{-1} \theta \hat{S} = \theta - i\eta$ and hence $\hat{S}^{-1} f(\theta) \hat{S} = f(\theta - i\eta)$ for any analytic functions f , while $\hat{S}^{-1} \hat{I} \hat{S} = \hat{I}$. Since \hat{S} commutes with the free-rotation factor, it follows that

$$\hat{U} = \hat{S}^{-1} \hat{U}_0 \hat{S}, \quad (139)$$

so that the \mathcal{PT} -symmetric Floquet operator is formally similar to a unitary one. At the purely algebraic level, this indicates that the quasi-energy spectrum can remain real, in which the quasi-energy is defined through the Floquet eigenvalue λ as $\lambda = e^{E_r + E_i}$ for the non-Hermitian case.

However, the mapping is physically meaningful only if the similarity transformation acts within the Hilbert space of normalizable states. In the angular-momentum basis $|m\rangle$ with $\hat{I}|m\rangle = m|m\rangle$, one has

$$\hat{S}|m\rangle = e^{\eta m}|m\rangle, \quad (140)$$

so the transformation exponentially reweights momentum components. Consequently, the mapping in Eq. (139) is meaningful only if the transformed Floquet eigenstates remain normalizable. This requirement marks the crucial distinction between nonresonant and resonant dynamics.

For the nonresonant regime, where the Hermitian kicked rotor \hat{U}_0 exhibits dynamical localization in angular momentum space, its Floquet eigenstates are exponentially localized: $|\phi_m^{(0)}\rangle \sim \exp(-|m - m_0|/\xi_L)$, with ξ_L the localization length. Under the transformation $|\phi_m^{(0)}\rangle \rightarrow \hat{S}^{-1}|\phi_m^{(0)}\rangle$, the amplitudes acquire a factor $e^{-\eta m}$, and remain normalizable provided the localization-induced decay dominates over the exponential reweighting. This yields the condition

$$\eta < \xi_L^{-1}, \quad (141)$$

which defines a finite \mathcal{PT} threshold γ_{PT} through $\eta = \text{artanh } \gamma$,

$$\gamma < \gamma_{\text{PT}} \sim \tanh(\xi_L^{-1}). \quad (142)$$

Consequently, in the dynamically localized regime there exists a genuine transition from an unbroken \mathcal{PT} phase (all quasi-energies real) to a broken \mathcal{PT} phase (complex-conjugate quasi-energy pairs). In this viewpoint, localization stabilizes the real Floquet spectrum by confining the support of eigenstates in momentum space, thereby keeping the non-unitary similarity transformation effectively bounded.

The resonance regime follows from the same criterion Eq. (142). However, at quantum resonance the Hermitian kicked rotor does not localize; Floquet eigenstates become extended in momentum space and the effective localization length diverges, $\xi_L \rightarrow \infty$. In this case the normalizability condition (141) cannot be satisfied for any nonzero η , so the similarity mapping (139) breaks down immediately. As a result, the Floquet spectrum becomes complex for arbitrarily small non-Hermiticity, so that the resonant rotor supports only the broken- \mathcal{PT} phase. This analysis is fully corroborated by the numerical results shown in Fig. 17.

An interesting dynamical consequence of the broken- \mathcal{PT} resonant dynamics is the emergence of ratchet acceleration in angular momentum space. Taking the principal quantum resonance as a representative example, where the kicking period satisfies $T = 4\pi$ and the Floquet operator simplifies to a purely kick-induced evolution,

$$\hat{U} = \exp[-iK(\cos \hat{\theta} + i\gamma \sin \hat{\theta})], \quad (143)$$

and expanding the complex kicking potential as

$$\cos \theta + i\gamma \sin \theta = \frac{1}{2}[(1 + \gamma)e^{i\theta} + (1 - \gamma)e^{-i\theta}], \quad (144)$$

we can observe that non-Hermiticity introduces an intrinsic asymmetry between forward and backward momentum-transfer channels. In contrast to the nonresonant case, where quantum interference suppresses long-range transport, at quantum resonance this asymmetry is not averaged out by localization effects.

The translational invariance of the resonant Floquet operator permits Bloch eigenstates labelled by a quasi-momentum q . The corresponding Floquet eigenvalues define a complex quasi-energy dispersion, whose imaginary part leads to mode-dependent amplification. As a result, the long-time dynamics is governed by the Bloch mode q^* that maximizes the imaginary part of the quasi-energy, i.e., the mode with the largest net gain. The real part of the dispersion then directly determines the transport properties of the selected mode. Consequently, generic initial states evolve toward a gain-selected Floquet mode

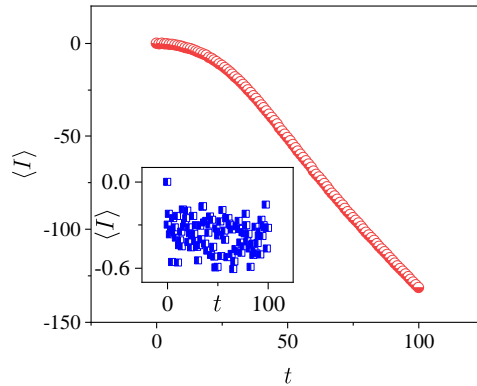


Fig. 18 Time evolution of the average momentum for $k = 3$ and $\gamma = 1/30$. Red circles correspond to $T = \pi/3$, and the inset shows the result for $T = 1$. (Adapted from [94].)

and develop a nonzero mean angular momentum (as confirmed in Fig. 18),

$$\langle I(t) \rangle = \frac{\langle \psi(t) | \hat{I} | \psi(t) \rangle}{\langle \psi(t) | \psi(t) \rangle} \sim vt, \quad (145)$$

Here the drift velocity v represents the group velocity of the gain-selected Bloch mode q^* .

Beyond the interplay between non-Hermiticity and quantum-interference phenomena such as dynamical localization and quantum resonance, non-Hermitian kicked rotors provide a natural and versatile framework for exploring quantum–classical correspondence in driven non-Hermitian systems [95]. Moreover, they have been employed to investigate how non-unitarity fundamentally alters the dynamics of out-of-time-ordered correlators [96, 97], universal spectral properties [98] and topological phases [68]. Taken together, these features establish the non-Hermitian kicked rotor as a minimal and powerful testbed for probing the interplay between chaos, topology, and gain-loss-induced mode selection in driven quantum systems.

4 Conclusion and Outlook

The kicked rotor stands as one of the most foundational paradigms in the theory of dynamical systems. Its enduring significance lies in the striking contrast between the extreme simplicity of its formulation and the exceptional richness of the dynamics it supports. Originally introduced as a minimal model of classical chaos, the kicked rotor has repeatedly re-emerged over the past decades as a universal reference system for exploring new physical phenomena, including quantum chaos, dynamical localization, Floquet topology, and non-Hermitian physics. Remarkably, this breadth is achieved without invoking disorder, interactions, or complex geometries: a single periodically kicked degree of freedom suffices to generate a hierarchy of dynamical regimes whose structure continues to shape our understanding of complex classical and quantum dynamics. It is precisely this combination of formal minimalism and conceptual universality that has established the kicked rotor as a cornerstone of modern nonequilibrium physics.

Given the breadth of the field, several important directions could not be covered in detail in the present review. For the original kicked rotor, we have not addressed the extensive body of work on spectral statistics [99] and their connection to random matrix theory, which provides a microscopic characterization of the transition from integrable to chaotic dynamics [100]. Closely related to this perspective are field-theoretical approaches [101, 102], including supersymmetric non-linear σ -models, which embed the kicked rotor within a broader universality framework traditionally associated with disordered systems. These formulations go beyond phenomenological descriptions and establish systematic links between microscopic dynamics, spectral correlations, and long-time transport properties. In addition, we have not discussed recent developments employing quantum correlation diagnostics, such as out-of-time-order correlators¹² [103], which have revealed new aspects of information scrambling and operator growth in kicked systems and lie beyond the scope of the present review. On the experimental side, we have also not covered recent studies that use the laser-kicked molecules platform to realize related investigations [104, 105].

For variants of the kicked rotor, we have touched on only a small subset of the many generalizations explored in the literature. Modifications of the driving protocol [106, 107, 108]—including alternative kicking sequences, quasi-periodic or aperiodic modulation, and more elaborate temporally structured drives—can significantly enrich the dynamical landscape.

¹²See I. García-Mata and D. A. Wisniacki, Quantum Analogues of Exponential Sensitivity: From Loschmidt Echo to Krylov Complexity, in this volume.

Such extensions establish connections to a range of phenomena, including discrete time crystals, anomalous transport, and forms of disorder engineered in the time domain. In parallel, interacting extensions of the kicked rotor introduce qualitatively new physics beyond the single-particle paradigm. In particular, the kicked Bose–Einstein condensate [109, 110] provides a natural and experimentally accessible bridge between quantum chaos and nonlinear mean-field dynamics. This system offers a controlled setting in which the role of interactions in shaping resonances, localization mechanisms, and dynamical stability can be systematically explored.

In the context of coupled kicked rotors, while we have discussed a concrete example at a conceptual level, a comprehensive treatment of the associated many-body phenomena lies beyond the scope of the present review and would require a separate and dedicated account. In recent years, substantial progress on many-body dynamical localization and delocalization in kicked and periodically driven systems [89, 90, 91, 111] has attracted intense interest, particularly in connection with ergodicity breaking, the stability of nonthermal phases, the mechanisms of thermalization in Floquet systems, and the relation to other many-body localized states found in lattice settings [82, 112]¹³.

Looking ahead, several research directions appear particularly promising. Many-body quantum chaos in driven systems is developing rapidly,¹⁴ and the many-body kicked rotor offers a rare opportunity to explore this regime while maintaining a clear connection to single-particle physics and semiclassical limits. Another important direction concerns dissipative quantum chaos [113, 114, 115]. Incorporating dissipation, decoherence, or measurement into kicked systems not only brings theoretical models closer to realistic experimental conditions, but also raises fundamental questions about the fate of localization, chaos, and universality in open quantum systems. In this context, the dissipative kicked rotor may serve as a minimal model for studying the competition between coherent chaotic dynamics and environmental effects.

More broadly, the continued relevance of the kicked rotor lies in its ability to connect and reinterpret emerging concepts from diverse areas of physics. As ideas from topology, non-Hermitian physics, quantum information, and nonequilibrium statistical mechanics continue to reshape our understanding of complex quantum systems, the kicked rotor provides a flexible and conceptually transparent platform on which these ideas can be explored, tested, and unified. Far from being an exhausted model, the kicked rotor remains a vibrant paradigm in which longstanding questions acquire fresh significance and genuinely novel phenomena continue to emerge.

Acknowledgments

G. B. acknowledges support from INFN through the project QUANTUM. J. G. acknowledges support by the National Research Foundation, Singapore through the National Quantum Office, hosted in A*STAR, under its Centre for Quantum Technologies Funding Initiative (No. S24Q2d0009).

References

- [1] I.P. Kornfeld, S.V. Fomin and Y.G. Sinai, *Ergodic Theory*, Springer-Verlag, New York (1982).
- [2] V. Alekseev and M. Yakobson, Symbolic dynamics and hyperbolic dynamic systems, *Physics Reports* **75** (1981) 290.
- [3] E. Ott, *Chaos in Dynamical Systems*, Cambridge University Press, Cambridge, UK, 2nd ed. (2002).
- [4] G. Casati, B.V. Chirikov and J. Ford, Marginal local instability of quasi-periodic motion, *Physics Letters A* **77** (1980) 91.
- [5] G. Casati, B.V. Chirikov, F.M. Izraelev and J. Ford, Stochastic behavior of a quantum pendulum under a periodic perturbation, in *Stochastic Behavior in Classical and Quantum Hamiltonian Systems*, G. Casati and J. Ford, eds., (Berlin, Heidelberg), pp. 334–352, Springer Berlin Heidelberg, 1979, DOI.
- [6] B.V. Chirikov, “Research concerning the theory of nonlinear resonance and stochasticity.” 1969.
- [7] B.V. Chirikov, A universal instability of many-dimensional oscillator systems, *Physics Reports* **52** (1979) 263.
- [8] G. Casati, B.V. Chirikov and D.L. Shepelyansky, Quantum limitations for chaotic excitation of the hydrogen atom in a monochromatic field, *Phys. Rev. Lett.* **53** (1984) 2525.
- [9] G. Casati, B.V. Chirikov, D.L. Shepelyansky and I. Guarneri, New photoelectric ionization peak in the hydrogen atom, *Phys. Rev. Lett.* **57** (1986) 823.
- [10] G. Casati, B.V. Chirikov, I. Guarneri and D.L. Shepelyansky, Dynamical stability of quantum “chaotic” motion in a hydrogen atom, *Phys. Rev. Lett.* **56** (1986) 2437.
- [11] G. Casati, I. Guarneri and D. Shepelyansky, Hydrogen atom in monochromatic field: chaos and dynamical photonic localization, *IEEE Journal of Quantum Electronics* **24** (1988) 1420.
- [12] J.E. Bayfield, G. Casati, I. Guarneri and D.W. Sokol, Localization of classically chaotic diffusion for hydrogen atoms in microwave fields, *Phys. Rev. Lett.* **63** (1989) 364.
- [13] F. Borgonovi, G. Casati and B. Li, Diffusion and localization in chaotic billiards, *Phys. Rev. Lett.* **77** (1996) 4744.
- [14] G. Casati and T. Prosen, The quantum mechanics of chaotic billiards, *Physica D: Nonlinear Phenomena* **131** (1999) 293.
- [15] G. Casati and T.c.v. Prosen, Triangle map: A model of quantum chaos, *Phys. Rev. Lett.* **85** (2000) 4261.
- [16] J. Wang, G. Benenti, G. Casati and W.-g. Wang, Quantum chaos and the correspondence principle, *Phys. Rev. E* **103** (2021) L030201.
- [17] J. Wang, G. Benenti, G. Casati and W.-g. Wang, Statistical and dynamical properties of the quantum triangle map, *Journal of*

¹³See J. Zakrzewski, Many-Body Localization, in this volume.

¹⁴See Andrey R. Kolovsky, Chaotic Dynamics and Quantum Transport, in this volume.

- [Physics A: Mathematical and Theoretical 55 \(2022\) 234002.](#)
- [18] V. Arnold and A. Avez, Ergodic Problems of Classical Mechanics, Advanced book classics, Addison-Wesley (1989).
- [19] A. Lichtenberg and M. Leiberman, Regular and Chaotic Dynamics, Applied Mathematical Sciences, Springer New York (2013).
- [20] J.M. Greene, A method for determining a stochastic transition, [Journal of Mathematical Physics 20 \(1979\) 1183.](#)
- [21] B.V. Chirikov, Time-dependent quantum systems, in Chaos and Quantum Physics, Les Houches Session LII, Elsevier Science Publishers (1989).
- [22] F.M. Izrailev, Simple models of quantum chaos: Spectrum and eigenfunctions, [Physics Reports 196 \(1990\) 299.](#)
- [23] F.M. Izrailev and D.L. Shepelyanski, Quantum resonance for a rotator in a nonlinear periodic field, *Theor. Math. Phys.* 43 (1980) 553.
- [24] I. Guarneri, On the spectrum of the resonant quantum kicked rotor, [Annales Henri Poincaré 10 \(2009\) 1097.](#)
- [25] G. Casati, J. Ford, I. Guarneri and F. Vivaldi, Search for randomness in the kicked quantum rotator, [Phys. Rev. A 34 \(1986\) 1413.](#)
- [26] G. Berman and G. Zaslavsky, Condition of stochasticity in quantum nonlinear systems, [Physica A: Statistical Mechanics and its Applications 91 \(1978\) 450.](#)
- [27] F. Chirikov, B. F.M. Izrailev and D.L. Shepelyanski, Dynamical stochasticity in classical and quantum mechanics, *Sov. Sci. Rev. C2* (1981) 209.
- [28] P.W. Anderson, Absence of diffusion in certain random lattices, [Phys. Rev. 109 \(1958\) 1492.](#)
- [29] P.A. Lee and T.V. Ramakrishnan, Disordered electronic systems, [Rev. Mod. Phys. 57 \(1985\) 287.](#)
- [30] S. Fishman, D.R. Grempel and R.E. Prange, Chaos, quantum recurrences, and anderson localization, [Phys. Rev. Lett. 49 \(1982\) 509.](#)
- [31] D.R. Grempel, R.E. Prange and S. Fishman, Quantum dynamics of a nonintegrable system, [Phys. Rev. A 29 \(1984\) 1639.](#)
- [32] J.E. Bayfield and P.M. Koch, Multiphoton ionization of highly excited hydrogen atoms, [Phys. Rev. Lett. 33 \(1974\) 258.](#)
- [33] P. Koch and K. van Leeuwen, The importance of resonances in microwave “ionization” of excited hydrogen atoms, [Physics Reports 255 \(1995\) 289.](#)
- [34] J.G. Leopold and I.C. Percival, Microwave ionization and excitation of rydberg atoms, [Phys. Rev. Lett. 41 \(1978\) 944.](#)
- [35] R.V. Jensen, Stochastic ionization of surface-state electrons, [Phys. Rev. Lett. 49 \(1982\) 1365.](#)
- [36] N.B. Delone, B.P. Kraïnov and D.L. Shepelyanskiï, Highly-excited atoms in the electromagnetic field, [Soviet Physics Uspekhi 26 \(1983\) 551.](#)
- [37] G. Casati, I. Guarneri and D. Shepelyansky, Classical chaos, quantum localization and fluctuations:, *Physica A* 163 (1990) 205–214.
- [38] F.L. Moore, J.C. Robinson, C.F. Bharucha, B. Sundaram and M.G. Raizen, Atom optics realization of the quantum δ -kicked rotor, [Phys. Rev. Lett. 75 \(1995\) 4598.](#)
- [39] B. Klappauf, W. Oskay, D. Steck and M. Raizen, Quantum chaos with cesium atoms: pushing the boundaries, [Physica D: Nonlinear Phenomena 131 \(1999\) 78.](#)
- [40] R. Graham, M. Schlautmann and P. Zoller, Dynamical localization of atomic-beam deflection by a modulated standing light wave, [Phys. Rev. A 45 \(1992\) R19.](#)
- [41] E. Abrahams, P.W. Anderson, D.C. Licciardello and T.V. Ramakrishnan, Scaling theory of localization: Absence of quantum diffusion in two dimensions, [Phys. Rev. Lett. 42 \(1979\) 673.](#)
- [42] G. Casati, I. Guarneri and D.L. Shepelyansky, Anderson transition in a one-dimensional system with three incommensurate frequencies, [Phys. Rev. Lett. 62 \(1989\) 345.](#)
- [43] J. Chabé, G. Lemarié, B. Grémaud, D. Delande, P. Szriftgiser and J.C. Garreau, Experimental observation of the anderson metal-insulator transition with atomic matter waves, [Phys. Rev. Lett. 101 \(2008\) 255702.](#)
- [44] G. Benenti, G. Casati, D. Rossini and G. Strini, Principles of Quantum Computation and Information (A Comprehensive Textbook), World Scientific Singapore (2019).
- [45] B. Georgeot and D.L. Shepelyansky, Exponential gain in quantum computing of quantum chaos and localization, [Phys. Rev. Lett. 86 \(2001\) 2890.](#)
- [46] G. Benenti, G. Casati, S. Montangero and D.L. Shepelyansky, Efficient quantum computing of complex dynamics, [Phys. Rev. Lett. 87 \(2001\) 227901.](#)
- [47] G. Benenti, G. Casati, S. Montangero and D.L. Shepelyansky, Dynamical localization simulated on a few-qubit quantum computer, [Phys. Rev. A 67 \(2003\) 052312.](#)
- [48] M.K. Henry, J. Emerson, R. Martinez and D.G. Cory, Localization in the quantum sawtooth map emulated on a quantum-information processor, [Phys. Rev. A 74 \(2006\) 062317.](#)
- [49] A. Pizzamiglio, S.Y. Chang, M. Bondani, S. Montangero, D. Gerace and G. Benenti, Dynamical localization simulated on actual quantum hardware, [Entropy 23 \(2021\) .](#)
- [50] S. Fishman, I. Guarneri and L. Rebuzzini, Stable quantum resonances in atom optics, [Phys. Rev. Lett. 89 \(2002\) 084101.](#)
- [51] S. Fishman, I. Guarneri and L. Rebuzzini, A theory for quantum accelerator modes in atom optics, [Journal of Statistical Physics 110 \(2003\) 911.](#)
- [52] M. Abb, I. Guarneri and S. Wimberger, Pseudoclassical theory for fidelity of nearly resonant quantum rotors, [Phys. Rev. E 80 \(2009\) 035206.](#)
- [53] M. Sadgrove, S. Wimberger, E. Arimondo, P.R. Berman and C.C. Lin, Chapter 7 - a pseudoclassical method for the atom-optics kicked rotor: from theory to experiment and back, in Advances In Atomic, Molecular, and Optical Physics, vol. 60, pp. 315–369, Academic Press (2011), [DOI.](#)
- [54] J. Wang, I. Guarneri, G. Casati and J. Gong, Long-lasting exponential spreading in periodically driven quantum systems, [Phys. Rev. Lett. 107 \(2011\) 234104.](#)
- [55] R. Artuso, F. Borgonovi, I. Guarneri, L. Rebuzzini and G. Casati, Phase diagram in the kicked Harper model, [Phys. Rev. Lett. 69 \(1992\) 3302.](#)
- [56] R. Artuso, G. Casati, F. Borgonovi, L. Rebuzzini and I. Guarneri, Fractal and dynamical properties of the kicked Harper model, [Int. J. Mod. Phys. B 08 \(1994\) 207.](#)
- [57] P. Fang and J. Wang, Superballistic wavepacket spreading in double kicked rotors, [Sci. China Phys. Mech. 59 \(2016\) 680011.](#)
- [58] L. Rebuzzini, I. Guarneri and R. Artuso, Spinor dynamics of quantum accelerator modes near higher-order resonances, [Phys. Rev. A 79 \(2009\) 033614.](#)
- [59] H. Wang, J. Wang, I. Guarneri, G. Casati and J. Gong, Exponential quantum spreading in a class of kicked rotor systems near high-order resonances, [Phys. Rev. E 88 \(2013\) 052919.](#)
- [60] Z. Zou and J. Wang, A pseudoclassical theory for the wavepacket dynamics of the kicked rotor model, [Sci. China Phys. Mech. 67](#)

- (2024) 230511.
- [61] Z. Zou and J. Wang, Pseudoclassical dynamics of the kicked top, *Entropy* 24 (2022) .
- [62] Z. Zou, J. Gong and W. Chen, Enhancing quantum metrology by quantum resonance dynamics, *Phys. Rev. Lett.* 134 (2025) 230802.
- [63] D.Y.H. Ho and J. Gong, Quantized adiabatic transport in momentum space, *Phys. Rev. Lett.* 109 (2012) 010601.
- [64] L. Zhou and J. Gong, Floquet topological phases in a spin-1/2 double kicked rotor, *Phys. Rev. A* 97 (2018) 063603.
- [65] Y. Koyama, K. Fujimoto, S. Nakajima and Y. Kawaguchi, Designing nontrivial one-dimensional Floquet topological phases using a spin-1/2 double-kicked rotor, *Phys. Rev. Res.* 5 (2023) 043167.
- [66] H. Wang, D.Y.H. Ho, W. Lawton, J. Wang and J. Gong, Kicked-Harper model versus on-resonance double-kicked rotor model: From spectral difference to topological equivalence, *Phys. Rev. E* 88 (2013) 052920.
- [67] R. Roy and F. Harper, Periodic table for Floquet topological insulators, *Phys. Rev. B* 96 (2017) 155118.
- [68] L. Zhou and J. Pan, Non-hermitian Floquet topological phases in the double-kicked rotor, *Phys. Rev. A* 100 (2019) 053608.
- [69] L. Zhou, Floquet second-order topological phases in momentum space, *Nanomaterials* 11 (2021) .
- [70] A.M. García-García and J. Wang, Universality in quantum chaos and the one-parameter scaling theory, *Phys. Rev. Lett.* 100 (2008) 070603.
- [71] W. Chen, G. Lemarié and J. Gong, Critical dynamics of long-range quantum disordered systems, *Phys. Rev. E* 108 (2023) 054127.
- [72] W. Chen, O. Giraud, J. Gong and G. Lemarié, Describing the critical behavior of the anderson transition in infinite dimension by random-matrix ensembles: Logarithmic multifractality and critical localization, *Phys. Rev. B* 110 (2024) 014210.
- [73] W. Chen, O. Giraud, J. Gong and G. Lemarié, Quantum logarithmic multifractality, *Phys. Rev. Res.* 6 (2024) L032024.
- [74] J.T. Edwards and D.J. Thouless, Numerical studies of localization in disordered systems, *Journal of Physics C: Solid State Physics* 5 (1972) 807.
- [75] A.M. García-García and J. Wang, Anderson transition in quantum chaos, *Phys. Rev. Lett.* 94 (2005) 244102.
- [76] G.M. Zaslavsky, Chaos, fractional kinetics, and anomalous transport, *Physics Reports* 371 (2002) 461.
- [77] A.D. Mirlin, Statistics of energy levels and eigenfunctions in disordered systems, *Physics Reports* 326 (2000) 259.
- [78] Y. Chen and C. Tian, Planck's quantum-driven integer quantum Hall effect in chaos, *Phys. Rev. Lett.* 113 (2014) 216802.
- [79] C. Tian, Y. Chen and J. Wang, Emergence of integer quantum Hall effect from chaos, *Phys. Rev. B* 93 (2016) 075403.
- [80] I. Guarneri, C. Tian and J. Wang, Self-duality triggered dynamical transition, *Phys. Rev. B* 102 (2020) 045433.
- [81] D.R. Grempel, S. Fishman and R.E. Prange, Localization in an incommensurate potential: An exactly solvable model, *Phys. Rev. Lett.* 49 (1982) 833.
- [82] D.A. Abanin, E. Altman, I. Bloch and M. Serbyn, Colloquium: Many-body localization, thermalization, and entanglement, *Rev. Mod. Phys.* 91 (2019) 021001.
- [83] S. Paul and A. Bäcker, Linear and logarithmic entanglement production in an interacting chaotic system, *Phys. Rev. E* 102 (2020) 050102.
- [84] F. Borgonovi and D.L. Shepelyansky, Enhancement of localization length for two interacting kicked rotators, *Nonlinearity* 8 (1995) 877.
- [85] M.O. Sales, W.S. Dias, A.R. Neto, M.L. Lyra and F.A.B.F. de Moura, Sub-diffusive spreading and anomalous localization in a 2d Anderson model with off-diagonal nonlinearity, *Solid State Communications* 270 (2018) 6.
- [86] M.B. Plenio and S. Virmani, An introduction to entanglement measures, *Quantum Information and Computation* 7 (2007) 1.
- [87] J. Gong and P. Brumer, Intrinsic decoherence dynamics in smooth hamiltonian systems: Quantum-classical correspondence, *Phys. Rev. A* 68 (2003) 022101.
- [88] S. Nag, A. Lahiri and G. Ghosh, Entropy production due to coupling to a heat bath in the kicked rotor problem, *Physics Letters A* 292 (2001) 43.
- [89] C. Rylands, E.B. Rozenbaum, V. Galitski and R. Konik, Many-body dynamical localization in a kicked Lieb-Liniger gas, *Phys. Rev. Lett.* 124 (2020) 155302.
- [90] J.H. See Toh, K.C. McCormick, X. Tang, Y. Su, X.-W. Luo, C. Zhang et al., Many-body dynamical delocalization in a kicked one-dimensional ultracold gas, *Nature Physics* 18 (2022) 1297.
- [91] A. Cao, R. Sajjad, H. Mas, E.Q. Simmons, J.L. Tanlimco, E. Nolasco-Martinez et al., Interaction-driven breakdown of dynamical localization in a kicked quantum gas, *Nature Physics* 18 (2022) 1302.
- [92] A. Russomanno, M. Fava and R. Fazio, Chaos and subdiffusion in infinite-range coupled quantum kicked rotors, *Phys. Rev. B* 103 (2021) 224301.
- [93] J.R. Schmidt, A. Bäcker and R. Ketzmerick, Classical drift in the Arnold web induces quantum delocalization transition, *Phys. Rev. Lett.* 131 (2023) 187201.
- [94] S. Longhi, Localization, quantum resonances, and ratchet acceleration in a periodically kicked \mathcal{PT} -symmetric quantum rotator, *Phys. Rev. A* 95 (2017) 012125.
- [95] J. Hall, S. Malzard and E.-M. Graefe, Semiclassical husimi distributions of Schur vectors in non-hermitian quantum systems, *Phys. Rev. Lett.* 131 (2023) 040402.
- [96] W.-L. Zhao, Quantization of out-of-time-ordered correlators in non-hermitian chaotic systems, *Phys. Rev. Res.* 4 (2022) 023004.
- [97] W.-L. Zhao, R.-R. Wang, H. Ke and J. Liu, Scaling laws of the out-of-time-order correlators at the transition to the spontaneous \mathcal{PT} -symmetry breaking in a floquet system, *Phys. Rev. A* 107 (2023) 062201.
- [98] G. Li, F. Chen and P. Fang, \mathcal{PT} -symmetry breaking and universal spectral statistics in quantum kicked rotors, *Phys. Rev. A* 110 (2024) 062221.
- [99] F. Izrailev, Quantum localization and statistics of quasienergy spectrum in a classically chaotic system, *Physics Letters A* 134 (1988) 13.
- [100] F. Haake, S. Gnutzmann and M. Kuś, Quantum Signatures of Chaos, Springer Series in Synergetics, Springer International Publishing, Cham, Switzerland, 4th ed. (2018).
- [101] A. Altland and M.R. Zirnbauer, Field theory of the quantum kicked rotor, *Phys. Rev. Lett.* 77 (1996) 4536.
- [102] C. Tian and A. Altland, Theory of localization and resonance phenomena in the quantum kicked rotor, *New Journal of Physics* 12 (2010) 043043.
- [103] E.B. Rozenbaum, S. Ganeshan and V. Galitski, Lyapunov exponent and out-of-time-ordered correlator's growth rate in a chaotic system, *Phys. Rev. Lett.* 118 (2017) 086801.
- [104] M. Bitter and V. Milner, Experimental demonstration of coherent control in quantum chaotic systems, *Phys. Rev. Lett.* 118 (2017) 034101.
- [105] V. Karle, A. Ghazaryan and M. Lemeshko, Topological charges of periodically kicked molecules, *Phys. Rev. Lett.* 130 (2023)

- 103202.
- [106] G. Casati, G. Mantica and D.L. Shepelyansky, Regular and anomalous quantum diffusion in the Fibonacci kicked rotator, [Phys. Rev. E 63 \(2001\) 066217](#).
 - [107] G. Abal, R. Donangelo, A. Romanelli, A.C. Sicardi Schifino and R. Siri, Dynamical localization in quasiperiodic driven systems, [Phys. Rev. E 65 \(2002\) 046236](#).
 - [108] F. Revuelta, R. Chacón and F. Borondo, Dynamical localization in nonideal kicked rotors driven by two competing pulsatile modulations, [Phys. Rev. E 110 \(2024\) 054202](#).
 - [109] C. Zhang, J. Liu, M.G. Raizen and Q. Niu, Transition to instability in a kicked Bose-Einstein condensate, [Phys. Rev. Lett. 92 \(2004\) 054101](#).
 - [110] J. Liu, C. Zhang, M.G. Raizen and Q. Niu, Transition to instability in a periodically kicked Bose-Einstein condensate on a ring, [Phys. Rev. A 73 \(2006\) 013601](#).
 - [111] Y. Guo, S. Dhar, A. Yang, Z. Chen, H. Yao, M. Horvath et al., Observation of many-body dynamical localization, [Science 389 \(2025\) 716](#).
 - [112] R.M. Nandkishore and S.L. Sondhi, Many-body localization with long-range interactions, [Phys. Rev. X 7 \(2017\) 041021](#).
 - [113] G.G. Carlo, G. Benenti and D.L. Shepelyansky, Dissipative quantum chaos: Transition from wave packet collapse to explosion, [Phys. Rev. Lett. 95 \(2005\) 164101](#).
 - [114] D. Villaseñor, L.F. Santos and P. Barberis-Blostein, Breakdown of the quantum distinction of regular and chaotic classical dynamics in dissipative systems, [Phys. Rev. Lett. 133 \(2024\) 240404](#).
 - [115] G. Passarelli, P. Lucignano, D. Rossini and A. Russomanno, Chaos and magic in the dissipative quantum kicked top, [Quantum 9 \(2025\) 1653](#).